2019-05-21

Low-Temperature Spin Seebeck Effect in the Helimagnetic Insulator Cu_2OSeO_3

Artem Akopyan
University of Miami, a.akopyan@outlook.com

UNIVERSITY OF MIAMI

LOW-TEMPERATURE SPIN SEEBECK EFFECT IN THE HELIMAGNETIC INSULATOR Cu_2OSeO_3

By

Artem Akopyan

A DISSERTATION

Submitted to the Faculty
of the University of Miami
in partial fulfillment of the requirements for
the degree of Doctor of Philosophy

Coral Gables, Florida

May 2019

UNIVERSITY OF MIAMI

A dissertation submitted in partial fulfillment of
the requirements for the degree of
Doctor of Philosophy

LOW-TEMPERATURE SPIN SEEBECK EFFECT IN THE HELIMAGNETIC INSULATOR Cu_2OSeO_3

Artem Akopyan

Approved:

_____ Joshua L. Cohn, Ph.D. Professor of Physics	_____ Fulin Zuo, Ph.D. Professor of Physics
_____ Sunxiang Huang, Ph.D. Assistant Professor of Physics	_____ Guillermo Prado, Ph.D. Dean of the Graduate School
_____ Jean-Hubert Olivier, Ph.D. Professor of Chemistry	

AKOPYAN, ARTEM (Ph.D., Physics)

Low-Temperature Spin Seebeck Effect in the Helimagnetic Insulator Cu_2OSeO_3 (May 2019)

Abstract of a dissertation at the University of Miami.
Dissertation supervised by Professor Joshua Cohn.
No. of pages in text. (80)

The rapidly growing fields of spin caloritonics and magnon spintronics have brought on a surge of interest in magnetic and thermal transport properties of magnetic insulators. Here we present low-temperature measurements of thermal conductivity and spin Seebeck effect in the helimagnetic insulator Cu_2OSeO_3 as functions of temperature, magnetic field, and crystallographic orientation. This compound hosts novel spin phases with long-period spin modulations, and its magnon thermal conductivity (~70 W/mK near 5 K) is the largest of any known ferro- or ferrimagnetic insulator. The magnetic field dependencies of thermal conductivity and spin Seebeck effect reveal novel aspects of phonon and magnon transport in chiral spin phases, like anisotropic scattering and domain structure. Analysis of the temperature dependence of spin Seebeck effect provides insight into the relevant time and length scales involved in thermally driven spin current phenomena.

DEDICATION

To my wife Ekaterina and daughter Arya

ACKNOWLEDGEMENT

I would like to express my gratitude to my advisor Dr. Joshua L. Cohn for the continuous support and guidance throughout the years.

I would like to thank my committee members Dr. Fulin Zuo, Dr. Sunxiang Huang, and Dr. Jean-Hubert Olivier for their helpful comments and interest in my research.

I would like to thank my wife Ekaterina and daughter Arya for their patience, love, and support during the preparation of this dissertation.

I am grateful to my parents for their support.

I would like to acknowledge the members of Dr. Cohn's research group Narayan Prasai, Saeed Moshfeghyeganeh, and Dharmendra Shukla for their companionship.

I also want to thank Anella Sebro for her help.

TABLE OF CONTENTS

LIST OF FIGURES

LIST OF TABLES

Chapter 1. Introduction

This chapter will summarize the historical development of the field of spin caloritonics and provide brief phenomenological descriptions of related concepts and effects.

1.1 Spin Hall Effect

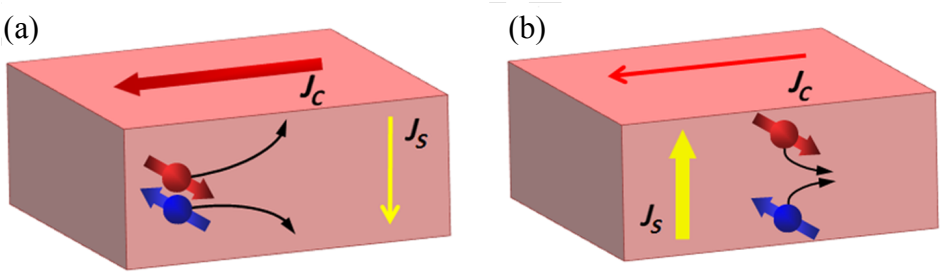

Figure 1.1 (from Ref. [1]). (a) Spin Hall effect: charge current (red arrow) induced a transverse spin current (yellow arrow), (b) inverse spin Hall effect: spin current (yellow arrow) induced a transverse charge current (red arrow).

Spin Hall effect refers to a conversion of a charge current density $\vec{J}_c$ into a transverse spin current density $\vec{J}_s$ as a result of spin-orbit interaction. The inverse effect is also possible and can be used to detect spin currents

$$\vec{E}_{ISHE} = \frac{2e}{\hbar}\theta_{SH}\,\vec{J}_s \times \vec{\sigma}. \tag{1.1}$$

where θ_{SH} is the spin Hall angle, $\vec{J}_s$ is the spin current, and $\vec{\sigma}$ is the spin direction.

1.2 Seebeck Effect

The first thermoelectric effect, the Seebeck effect, was discovered by Thomas Seebeck in 1821 [2] and involved interactions between heat currents and charge currents. Seebeck effect refers to a generation of a charge current in a material in response

to a temperature gradient. Microscopically, under open circuit conditions charge carriers at the hot end diffuse towards the cold end until the electric field within the material is established through carrier accumulation and equilibrium is reached (Figure 1.2). Then the Seebeck coefficient S is defined as

$$S = -\frac{V_{SE}}{\Delta T}. \tag{1.2}$$

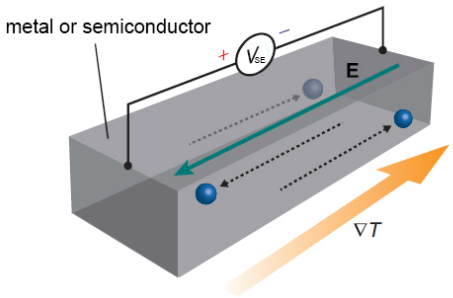

Figure 1.2 (from Ref. [1]). Illustration of Seebeck effect.

This concept found applications in many modern devices like thermometers, coolers, power generators, waste heat recyclers and many more.

1.3 Spin Seebeck Effect

In spin Seebeck effect (SSE) heat currents interact with spin waves (magnons) and inverse spin Hall effect is used to detect these thermally driven spin currents. The simplest system involves a ferromagnetic insulator in interfacial contact with a paramagnetic, heavy metal. Two configurations are possible: longitudinal and transverse (Figure 1.3). In the more straight forward longitudinal configuration, when magnetization is perpendicular to the temperature gradient, the temperature gradient produces a magnon spin current that results in magnon accumulation at the cold end. Experimentally, the spin accumulation is detected by a placement of a thin paramagnetic film on the surface perpendicular to the

heat flow. Magnon accumulation pumps spin current into the film, where it is converted to an electrically detectable charge current via the inverse spin Hall effect [1], [4].

In the transverse configuration (Figure 1.3b), the temperature gradient is applied along the x direction. In order to generate an ISHE voltage, the ferromagnet has to be magnetized along the direction of the gradient. Therefore, the anomalous Nernst effect in the ferromagnet vanishes, since magnetization and ΔT are collinear, enabling an unperturbed detection of the transverse SSE in various magnetic materials. The characteristic property of the transverse SSE is the sign reversal of the thermally generated spin voltage between the lower and higher temperature ends of the ferromagnet.

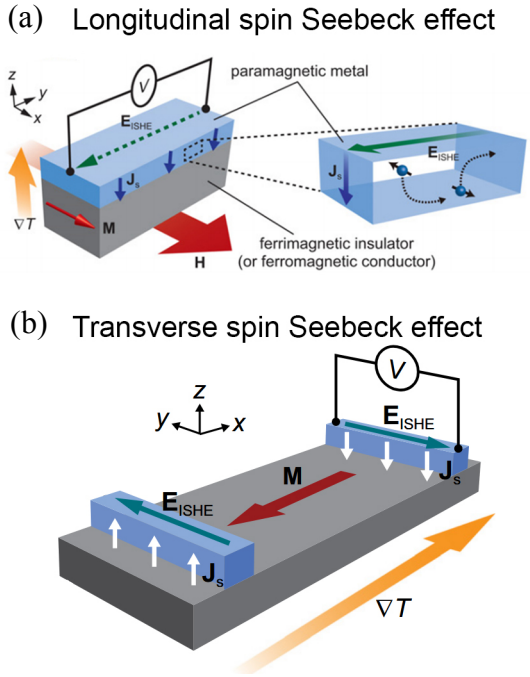

Figure 1.3 (from Ref.[1], [4]). Two possible SSE configurations.

Spin Seebeck was first experimentally observed by Uchida *et al.* in 2008 [3]. The measurements were done on thick permalloy ($Ni_{81}Fe_{19}$) films with platinum strips for SSE detection in the transverse configuration. Subsequently, spin Seebeck was observed in insulators [5] and semiconductors [6].

Xiao *et al.* [7] provided the first theoretical description of SSE bases on interfacial spin pumping driven by the difference between phonon temperature and magnon temperature. Agrawal *et al.* [8] directly measured the temperature of short wavelength magnons in YIG with Brillouin light scattering technique. They observed a difference between phonon and magnon temperatures that is much smaller than the one predicted by Xiao *et al.* Kehlberger *et al.* [93] reported that the thickness dependence of spin Seebeck effect in YIG films correlated with the bulk magnon mean free path, suggesting that thermally driven magnons in the bulk, rather than the interface, are responsible for spin Seebeck effect. This origin of SSE has been corroborated by recent theoretical and experimental work [68].

Chapter 2. Theoretical Background

This chapter will present brief summaries of theories and models used in the analysis of thermal conductivity and spin Seebeck data in Chapters 5 and 6. We will limit this overview only to physical phenomena relevant to magnetic insulators, where the only energy carriers and phonons and magnons.

2.1 Lattice Thermal Conductivity

2.1.1 Phonons

A phonon is a quantum mechanical representation of a vibrational mode of atoms in a periodic lattice. Phonons are the primary quasiparticles that are responsible for thermal conductivity of the lattice, so they play a central role in heat transport of insulators [9]. Phonons are bosons and obey Bose-Einstein statistics with the equilibrium distribution

$$n_k^0 = \frac{1}{\exp\left(\frac{\hbar\omega_k}{k_B T}\right) - 1}. \tag{2.1}$$

Phonon group velocity is given by $\vec{v}_k = \nabla_k \omega_k$ and the dispersion relation is approximately linear for small wave numbers, $\omega_k = v_k k$).

In the presence of a temperature gradient, the distribution drifts away from equilibrium at a rate

$$\left(\frac{\partial n_k}{\partial t}\right)_{drift} = -\vec{v}_k \cdot \nabla\, n_k = -\vec{v}_k \cdot \nabla T \frac{dn_k}{dT}, \tag{2.2}$$

and in the steady state must be opposite of the change due to phonon scattering, resulting in Boltzmann equation

$$\left(\frac{\partial n_k}{\partial t}\right)_{scattering} - \vec{v}_k \cdot \nabla T \frac{dn_k}{dT} = 0. \tag{2.3}$$

Two approximations are used to solve this equation. First, only the n_k^0contribution is kept in

$$\frac{\partial n_k}{\partial T} \approx \frac{\partial n_k^0}{\partial T}. \tag{2.4}$$

Secondly, the relaxation time approximation assumes that when the deviations from the equilibrium are small, the scattering term can be expressed by

$$\left(\frac{\partial n_k}{\partial t}\right)_{scattering} = \frac{n_k^0 - n_k}{\tau_k} = -\frac{\delta n_k}{\tau_k}, \tag{2.5}$$

where τ_k is the relaxation time and δn_k is the phonon number in excess of equilibrium. With these approximations, the Boltzmann equation describing phonon dynamics assumes the form

$$-\tau_k \vec{v}_k \cdot \nabla T \frac{\partial n_k^0}{\partial T} = \delta n_k. \tag{2.6}$$

Substituting the result into the expression for the heat current due to a flow of phonons gives (summation over phonon branches is implied)

$$\begin{aligned} \vec{J}_{Q,p} &= \frac{1}{(2\pi)^3}\int d^3k\, \delta n_k \hbar\omega_k \vec{v}_k = -\frac{1}{(2\pi)^3}\int d^3k\, \hbar\omega_k \vec{v}_k^2 \tau_k \frac{\partial n_k^0}{\partial T} \nabla T \\ &= -\kappa_L \nabla T. \end{aligned} \tag{2.7}$$

Thus, assuming linear dispersion $\omega_k = v_k k$, averaging over the phonon branches (v – averaged velocity), and using the maximum frequency of the vibrational spectrum (given by Debye temperature θ_D) one obtains the phonon thermal conductivity

$$\kappa_L = \frac{k_B}{2\pi^2 v}\int_0^{k_B\theta_D/\hbar} \omega^2 \tau(\omega, T)\left(\frac{\hbar\omega}{k_B T}\right)^2 \frac{e^{\frac{\hbar\omega}{k_B T}}}{\left(e^{\frac{\hbar\omega}{k_B T}} - 1\right)^2} d\omega. \tag{2.8}$$

With an introduction of a dimensionless variable $x = \frac{\hbar\omega}{k_B T}$, this becomes

$$\begin{aligned}\kappa_L &= \frac{k_B}{2\pi^2 v}\left(\frac{k_B T}{\hbar}\right)^3 \int_0^{\theta_D/T} \tau(x, T)\frac{x^4 e^x}{(e^x - 1)^2} dx \\ &= \frac{1}{3}\int_0^{\theta_D/T} C(x)\, v^2 \tau(x) dx,\end{aligned} \tag{2.9}$$

where

$$C_p(x) = \frac{3k_B}{2\pi^2 v^3}\left(\frac{k_B T}{\hbar}\right)^3 \frac{x^4 e^x}{(e^x - 1)^2} \tag{2.10}$$

is the contribution to heat capacity from phonons of frequency $\omega = \frac{k_B T x}{\hbar}$. In this relaxation time approximation, all scattering processes are treated on equal grounds in the context of Matthiessen's rule that says that rates due to different scattering mechanisms τ_i^{-1} contribute equally to the total relaxation rate

$$\tau^{-1} = \sum_i \tau_i^{-1}. \tag{2.11}$$

2.1.2 Phonon Scattering Mechanisms

Intrinsic Scattering

For real crystal lattices the harmonic approximation is not exactly valid, therefore, one needs to consider the effects of anharmonic forces, that play a crucial role in the theory of thermal transport. Indeed, in a perfectly harmonic, defect-free lattice, there would be no scattering mechanisms for phonons, resulting in an infinite thermal conductivity. Anharmonicity introduces phonon-phonon scattering into the picture. Generally, only

three-phonon processes are relevant at low temperatures. Scattering theory, first introduced by Pierels [9], finds that energy and momentum conservation considerations imply the rate of change of phonon distribution due to scattering event between three phonons with frequencies and reduced wave vectors in the first primitive cell ω_i and $\vec{k}_i$ vanishes, unless the following conditions are satisfied (in the case of coalescence)

$$\omega_1 + \omega_2 = \omega_3$$
$$\text{and} \qquad \vec{k}_1 + \vec{k}_2 = \vec{k}_3, \text{ or } \vec{k}_1 + \vec{k}_2 = \vec{k}_3 + \vec{K} \tag{2.12}$$

where $\vec{K}$ is the reciprocal lattice vector. Eq. (2.12) suggests that there are two distinct processes, although this distinction depends on the choice of the primitive cell [10]. Historically, the $\vec{k}$ conserving process are called normal processes, while the non-conserving processes are called Umklapp processes. Peierls has also shown that normal processes alone (i.e. no other scattering is present) do not completely relax the phonon distribution and, therefore, produce a non-zero heat flux even in the absence of a thermal gradient, but together with Umklapp processes they shape the thermal conductivity throughout the temperature range. Normal processes help to establish equilibrium between low and high frequency phonons, ultimately, slightly changing the phonon distribution and having a moderate effect on the overall thermal conductivity at low temperatures in some models. Recent *ab-initio* first principle calculations reveal that even at room temperatures a big fraction of thermal conductivity is attributable to low frequency phonons that scatter though normal processes [11].

The derivation of the intrinsic scattering processes is based on the treatment of the anharmonic interaction in the framework of first Born approximation and the calculation

of transition probabilities between two phonon states and, therefore, rates of change of the phonon distribution [12].

In general, the scattering rate for normal processes has the form

$$\tau_N^{-1} = A\omega^{\alpha^N} T^{\beta^N} \tag{2.13}$$

where A is a free parameter, $\alpha^N = 2$, $\beta^N = 3$ at low temperatures, and $\alpha^N = 2$, $\beta^N = 1$ in the high temperature limit [13]. Various authors calculated or derived from experimental data the following form for the Umklapp scattering rate

$$\tau_U^{-1} = B\omega^{\alpha^U} T^{\beta^U} \exp\left(-\theta_D / bT\right) \tag{2.14}$$

where B and b are free parameters, $\alpha^U = 2$, $\beta^N = 3$ [14], [15].

Extrinsic Scattering

Phonons can scatter from crystal boundaries, lattice defects and impurities, as well as other quasiparticles participating in thermal transport.

The scattering rate of phonons due to crystal boundaries of a rod-like sample is due to the original work of Casimir [16]

$$\tau_B^{-1} = \frac{v}{l_0} = \frac{v}{2\sqrt{a/\pi}}, \tag{2.15a}$$

$$\kappa_L = \left(\frac{2\pi^2}{15}\right)\left(\frac{k_B T}{\hbar}\right)^3 k_B v l_{ph} \tag{2.15b}$$

where l_0 is the transverse dimension of the rod, a is the cross-sectional area, l_{ph} − phonon mean-free path. Phonon thermal conductivity in boundary limited regime (ballistic transport) is given in Equation 2.15b.

The expression for the scattering from impurities or point defects was derived by Klemens [17]

$$\tau_i^{-1} = n\frac{V_0}{4\pi v^3}\omega^4\left\{\left(\frac{\Delta M}{M}\right)^2 + 2\left[\frac{\Delta F}{F} - 13.44\left(\frac{\Delta R}{R}\right)^2\right]\right\}, \tag{2.16}$$

where n is the impurity concentration, V_0 is the unit cell volume, ΔM is the mass difference between host and impurity atom, M is the average molecular mass, ΔF is the change in the force constant, ΔR is the change in the nearest neighbor distance. In the case of vacancies, Eq. (2.16) reduces to

$$\tau_v^{-1} = n\frac{9a^3}{4\pi v^3}\omega^4\left(\frac{M_v}{M}\right)^2, \tag{2.17}$$

where a is the atomic radius and M_v is the atomic mass of the vacant atom [18]. This concludes our overview of most common phonon scattering mechanisms; other mechanisms not included here are isotope scattering, sheet like defects, grain boundaries, resonant spin scattering, etc. Phonon-magnon interactions will be discussed in more detail in Section 2.2.2.

2.1.3 Beyond the Relaxation Time Approximation

J. Callaway introduced a model for lattice thermal conductivity that makes an effort to better account for the effects of normal scattering processes on thermal conductivity at low temperatures [19]. In his model, Callaway follows Ref. [20] and uses the concept of a displaced (or "flowing equilibrium") distribution

$$n_k^* = \left[\exp\left(\frac{\hbar\omega_k - \vec{\lambda}\cdot\vec{k}}{k_B T}\right) - 1\right]^{-1} = n_k^0 + \frac{\vec{\lambda}\cdot\vec{k}}{k_B T}\frac{e^{\hbar\omega_k/k_B T}}{(e^{\hbar\omega_k/k_B T} - 1)^2}. \tag{2.18}$$

This is the distribution normal processes relax to in the absence of other scattering. The rate of change of the distribution due to collisions then takes the form

$$\left(\frac{\partial n_k}{\partial t}\right)_{scattering} = \frac{n_k^0 - n_k}{\tau_k^U} + \frac{n_k^* - n_k}{\tau_k^N}, \tag{2.19}$$

where τ_k^N is the relaxation rate due to normal processes, τ_k^U is the sum of all momentum non-conserving rates, and the combined relaxation rate is

$$\tau_C^{-1} = \tau_N^{-1} + \tau_U^{-1}\,. \tag{2.20}$$

Substituting this in the Boltzmann equation (Eq. 2.3) and accounting for the correction by P. Allen [21] leads to the final expression for lattice thermal conductivity

$$\kappa_L = \frac{k_B}{2\pi^2 v}\left(\frac{k_B T}{\hbar}\right)^3 \int_0^{\theta_D/T} \tau_C(x,T)\frac{x^4 e^x}{(e^x-1)^2}\,dx\left[1 + \frac{\overline{\tau_C(x,T)/\tau_N(x,T)}}{\overline{\tau_C(x,T)/\tau_U(x,T)}}\right], \tag{2.21}$$

where

$$\overline{f(T)} = \int_0^{\theta_D/T} f(x,T)\frac{x^4 e^x}{(e^x-1)^2}\,dx \Big/ \int_0^{\theta_D/T} \frac{x^4 e^x}{(e^x-1)^2}\,dx\,. \tag{2.22}$$

2.2 Magnon Thermal Conductivity

2.2.1 Magnons

A magnon is a quantum mechanical representation of a collective excitation of spins (spin wave) in a periodic lattice. Like phonons, magnons obey the Bose-Einstein statistics (Eq. 2.1), but their dispersion relation is approximately quadratic for small wave numbers, $\omega_k = (D/\hbar)k^2$, where D is the spin-wave stiffness. The presence of magnons in a magnetic insulator can significantly affect its thermal conductivity as magnons can carry energy and contribute to the total thermal conductivity or reduce it by scattering phonons. Following the transport theory outlined in Section 2.1.1, the thermal conductivity due to non-equilibrium magnons driven by a temperature gradient can be calculated by

$$\kappa_m = \frac{k_B}{6\pi^2}\int_0^{k_m} k^2\,\tau_k\,v_k^2\,\frac{x^2e^x}{(e^x-1)^2}\,dk \tag{2.23a}$$

$$\kappa_m = \frac{\zeta(3)k_B^3 l_m}{4\pi^2\hbar D}T^2 \tag{2.23b}$$

where k_m is the maximum magnon wave number under the assumption of a spherically symmetric dispersion, τ_k is the relaxation time of magnons with wave number k, and $x = \frac{\hbar\omega}{k_B T}$. In the boundary-limited regime, magnon heat conduction reduces to Eq. 2.23b [22]. Using an approximation for the magnon dispersion relation suitable for large wave numbers $\omega_k = \omega_{ZB}(1-\cos\pi k/2k_m)$ and introducing a normalized wave number $q = k/k_m$ [23], the thermal conductivity becomes

$$\kappa_m = \frac{\omega_{ZB}^2 k_m k_B}{24}\int_0^1 q^2 sin^2\left(\frac{\pi q}{2}\right)\tau_q\,\frac{x^2e^x}{(e^x-1)^2}\,dq. \tag{2.24}$$

2.2.2 Magnon Scattering

Theory of magnon interactions in the first Born approximation has been studied in great detail by Akhiezer *et. al.* in Ref. [24]. They estimate the scattering rates due to normal 3-magnon confluence $\tau_{3N,c}^{-1}$ and splitting $\tau_{3N,s}^{-1}$as well as 4-magnon scattering events τ_{4N}^{-1} for a magnon with wavenumber k:

$$\tau_{3N,c}^{-1}(k) \approx \left(\frac{g\mu_B M_s}{2\pi\theta_C}\right)^2 \frac{k_B T}{\hbar}\,\frac{\theta_C}{\Delta}\,ak, \tag{2.25a}$$

$$\tau_{3N,s}^{-1}(k) \approx \left(\frac{g\mu_B M_s}{\theta_C}\right)^2 \frac{k_B T}{6\pi\hbar}\left(\frac{\theta_C}{\Delta}\right)^{1/2}\left(\frac{\varepsilon(k)}{\Delta}-3\right)^{1/2}, \tag{2.25b}$$

$$\tau_{4N}^{-1}(k) \approx \frac{\theta_C}{\hbar}\left(\frac{k_B T}{\theta_C}\right)^{5/2}(ak)^3, \tag{2.25c}$$

where g is the gyromagnetic ratio, μ_B – Bohr magneton, M_s – saturation magnetization, a – lattice parameter, and $\varepsilon(k) = \Delta + \theta_C(ak)^2$ is the magnon dispersion relation. Forney and Jackle [25] used a similar approach to calculate thermally averaged 3-magnon and 4-magnon normal (τ_{3N}^{-1}, τ_{4N}^{-1}) and Umklapp (τ_{3U}^{-1}, τ_{4U}^{-1}) scattering rates and magnon-impurity scattering rate (τ_i^{-1}):

$$\tau_{3N}^{-1} = 2.6\frac{k_B}{\hbar}{T_d}^2{T_e}^{-3/2}T^{1/2}, \qquad \tau_{4N}^{-1} = 6.1\times10^4\frac{k_B}{S^2\hbar}{T_e}^{-3}T^4,$$

$$\tau_{3U}^{-1} = 1.4\times10^4\frac{Sk_B}{\hbar}{T_d}^2{T_e}^{-1/2}T^{-1/2}exp(-12T_e/T), \tag{2.26}$$

$$\tau_{4U}^{-1} = \frac{2k_B}{\hbar S^2}{T_e}^{-1/2}T^{3/2}exp(-12T_e/T),$$

$$\tau_i^{-1} = 0.4c\frac{{k_B}^2}{\hbar}{T_e}^{-3/2}T^{5/2},$$

where

$$T_d = \frac{(g\mu_B)^2}{k_B a^3}, \qquad T_e = \frac{2SJ}{k_B},$$

and S is the effective spin, J is the exchange coupling constant, and c is the impurity concentration.

2.3 Spin Seebeck Effect

This section will outline the bulk magnon spin current theory for the longitudinal spin Seebeck effect [26]-[28]. This approach proposes that the thermal flow of magnons in the bulk of the insulator creates an accumulation of magnons at the interface between a ferromagnetic or ferrimagnetic insulator (FMI) and a metallic layer (ML). The magnon accumulation enables the mechanism of spin pumping into the ML layer. Spin pumping

creates a spin current, which is converted to a charge current by inverse spin Hall effect in the ML layer. The entire process is illustrated in Fig. 2.1.

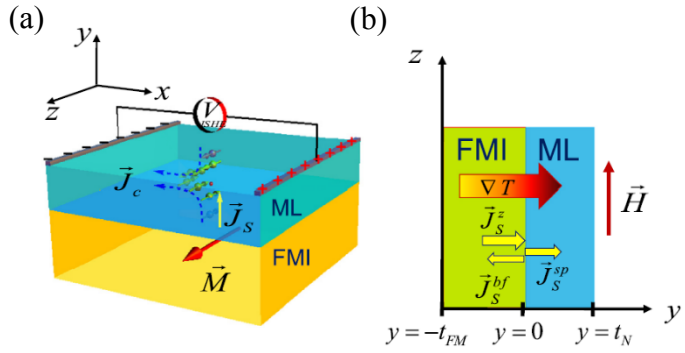

Figure 2.2 (from Ref. [27]). (a) Schematic illustration of the FMI/ML heterostructure and spin-to-charge current conversion in the ML. (b) Diagram showing temperature gradient induced and back-flow spin currents in the FMI and the pumped spin current in the ML.

Using the approach established in Section 2.1.1, the magnon accumulation at the FMI/ML interface is defined as the density of magnons in excess of equilibrium

$$\delta n_m(\vec{r}) = \frac{1}{(2\pi)^3}\int d^3k\,[n_k(\vec{r}) - n_k^0]. \tag{2.27}$$

The bulk magnon spin current density with polarization z is

$$\vec{J}_s^z = \frac{\hbar}{(2\pi)^3}\int d^3k\,\vec{v}_k[n_k(\vec{r}) - n_k^0]. \tag{2.28}$$

Using the Boltzmann equation for magnons

$$-\tau_k\vec{v}_k\cdot\nabla n_k(\vec{r}) = n_k(\vec{r}) - n_k^0 \tag{2.29}$$

and plugging into Eq. (2.28) gives two contributions to the spin current $\vec{J}_s^z = \vec{J}_{S\nabla T}^z + \vec{J}_{S\delta n}^z$, where

$$\vec{J}_{S\nabla T}^z = -\frac{\hbar}{(2\pi)^3}\int d^3k\,\tau_k\frac{\partial n_k^0}{\partial T}\vec{v}_k(\vec{v}_k\cdot\nabla T) \tag{2.30}$$

is due to temperature gradient driven flow of magnons and

$$\vec{J}^z_{S\delta n} = -\frac{\hbar}{(2\pi)^3}\int d^3k\,\tau_k\vec{v}_k[\vec{v}_k\cdot\nabla(n_k(\vec{r})-n_k^0)] \tag{2.31}$$

is due to spatial variation of magnon accumulation. The first contribution evaluates to

$$\vec{J}^z_{S\nabla T} = -\left[\frac{\hbar}{(2\pi)^3 T}\int d^3k\,\tau_k v^2_{k,y}\frac{xe^x}{(e^x-1)^2}\right]\nabla T, \tag{2.32}$$

where $x = \frac{\hbar\omega_k}{k_B T}$ and the temperature gradient is normal to the interface (in the +y direction). In order to calculate the contribution to the total spin current due to magnon accumulation, an approximate solution to Boltzmann equation (Eq. 2.29) is required. The magnon distribution function is written as a sum of the equilibrium distribution and a small deviation, $n_k(\vec{r}) = n_k^0[1+\hbar\omega_k g(y)]$, where $g(y)$ is determined by the solution of the boundary value problem. Substituting into Eq. 2.27, the magnon accumulation becomes

$$\delta n_m(y) = \frac{1}{(2\pi)^3}\int d^3k\,n_k^0\hbar\omega_k g(y). \tag{2.33}$$

Plugging the result into Eq. 2.31 gives the spin current due to magnon accumulation

$$\vec{J}^z_{S\delta n}(y) = -\hbar D_m\frac{\partial}{\partial y}\delta n_m(y), \tag{2.34}$$

where

$$D_m = \int d^3k\,\tau_k v^2_{k,y} n_k^0\hbar\omega_k \Big/ \int d^3k\,n_k^0\hbar\omega_k \tag{2.35}$$

is the magnon diffusion coefficient. Since the magnon accumulation relaxes through magnon-phonon interactions with a relaxation time τ_{mp}, the conservation of angular momentum implies $\frac{\partial \vec{J}^z_S}{\partial y} = -\hbar\frac{\delta n_m(y)}{\tau_{mp}}$, resulting in a diffusion equation for magnon accumulation

$$\frac{\partial^2\delta n_m(y)}{\partial y^2} = \frac{\delta n_m(y)}{l_m^2}, \tag{2.36}$$

where $l_m = \left(D_m \tau_{mp}\right)^{1/2}$ is the magnon diffusion length. Solving Eq. 2.36 and substituting in Eq. 2.34 results in the spin current density

$$\vec{J}^z_{S\delta n}(y) = -\hbar \frac{D_m}{l_m} A e^{\frac{y}{l_m}} + \hbar \frac{D_m}{l_m} B e^{-y/l_m}, \tag{2.37}$$

where A and B are coefficients determined by boundary conditions.

The next step is to calculate the spin current that enters the ML. In the presence of an external magnetic field and spin accumulation at the FMI/ML interface, the magnetization of the FMI $\vec{M}$ will precess and result in spin pumping into the ML. The resulting spin current is given by

$$\vec{J}^{sp}_S(0^+) = \frac{\hbar g_r^{\uparrow\downarrow}}{4\pi M^2}\left(\vec{M} \times \frac{\partial \vec{M}}{\partial t}\right), \tag{2.38}$$

where $g_r^{\uparrow\downarrow}$ is the real part of spin mixing conductance [29], [30]. This spin current can be expressed in terms of the spin accumulation as follows

$$\begin{aligned} \vec{J}^z_S(0^+) = -\frac{\hbar g_{eff}^{\uparrow\downarrow}}{4\pi M^2} \sum_k \omega_k (m_k^+ m_k^-) \approx \\ -\frac{\gamma \hbar^2 g_{eff}^{\uparrow\downarrow}}{2\pi M} \delta n_m(0) \left[\frac{\int d^3k n_k^0 \hbar \omega_k^2}{\int d^3k\, n_k^0 \hbar \omega_k}\right]. \end{aligned} \tag{2.39}$$

Here m_k^+ and m_k^- are the transverse components of the magnetization of the magnon with wave vector k, $g_{eff}^{\uparrow\downarrow}$ is the real part of the effective spin mixing conductance that accounts for the backflow spin current, and the linear approximation $m_k^+ m_k^- = 2M\gamma\hbar\delta n_k/V$ has been used. The conservation of angular momentum current imposes boundary conditions that are used to calculate coefficients A and B in Eq. 2.37. The resulting spin current at the interface can be shown to take the following approximate form

$$\vec{J}_S^z(0) = -\left[\frac{\gamma\hbar g_{eff}^{\uparrow\downarrow}\tau_{mp}^{1/2}}{2\pi M}\frac{\cosh(t_{FM}/l_m)-1}{\sinh(t_{FM}/l_m)}\frac{\int d^3k\, n_k^0\hbar\omega_k^2\frac{\hbar}{T}\int d^3k\,\tau_k v_{k,y}^2\frac{xe^x}{(e^x-1)^2}}{\int d^3k\, n_k^0\hbar\omega_k\int d^3k\,\tau_k v_{k,y}^2 n_k^0\hbar\omega_k}\right]\nabla T, \qquad (2.40)$$

This spin current enters the ML and generates a charge current in the x-direction as a result of the inverse spin Hall effect $\vec{J}_c = \theta_{SH}(2e/\hbar)\vec{J}_S^z \times \vec{\sigma}$, where θ_{SH} is the spin Hall angle and $\vec{\sigma}$ is the spin polarization [31]. Using the more accurate (for big k) magnon dispersion relation $\omega_k = \omega_{ZB}(1-\cos\pi k/2k_m)$, a normalized wave number $q = k/k_m$ and normalized relaxation rate $\eta_q = \tau_0/\tau_k$, where τ_0 is the relaxation time of $k \approx 0$ magnons, and integrating the charge current density one obtains the voltage at the ends of the metal layer

$$V_{LSSE} = R_N w\lambda_N\frac{2e}{\hbar}\theta_{SH}tanh\left(\frac{t_N}{2\lambda_N}\right)\frac{B_1B_s}{(B_0B_2)^{1/2}}\mathrm{F}\,\rho\, g_{eff}^{\uparrow\downarrow}\nabla T, \qquad (2.41)$$

where R_N, t_N, w are the resistance, thickness, and width of the metal film, and λ_N is the spin diffusion length in the metal film. Material parameter F, and B integrals are given by

$$F = \frac{\gamma\hbar k_B\tau_{mp}^{1/2}\tau_0^{1/2}k_m^2\omega_{ZB}}{8\sqrt{3}\pi^2 M},$$

$$B_s = \int_0^1 dq\, q^2 sin^2\left(\frac{\pi q}{2}\right)\frac{xe^x}{\eta_q(e^x-1)^2}, \qquad B_1 = \int_0^1 dq\, q^2\frac{x^2}{e^x-1}, \qquad (2.42)$$

$$B_2 = \int_0^1 dq\, q^2 sin^2\left(\frac{\pi q}{2}\right)\frac{x}{\eta_q(e^x-1)}, \qquad B_0 = \int_0^1 dq\, q^2\frac{x}{e^x-1}.$$

Chapter 3. Experimental Methods

This chapter will focus on multiple experimental techniques, procedures, and equipment utilized in preparation and characterization of samples and employed to set up and carry out various low-temperature measurements. X-ray diffraction characterization techniques will be covered first, followed by a summary of sample preparation techniques. Then we will cover the use of dc magnetron sputtering in deposition of thin films on surfaces of bulk samples, do an overview of experimental setups employed in various transport measurements, and finish by outlining the data collection procedures.

3.1 X-ray Diffraction (XRD)

3.1.1 Theory of Operation

X-rays are electromagnetic radiation of wavelength ranging between 0.1 and 100 Å. The most common way to produce X-rays in a lab environment is to use an X-ray tube – a vacuum tube with a voltage between the cathode and the anode high enough to accelerate the elections and make them collide with the anode (typically made of tungsten, molybdenum or copper). If the tube voltage is above the critical value, in addition to continuous bremsstrahlung radiation, sharp high intensity peaks, called characteristic lines,

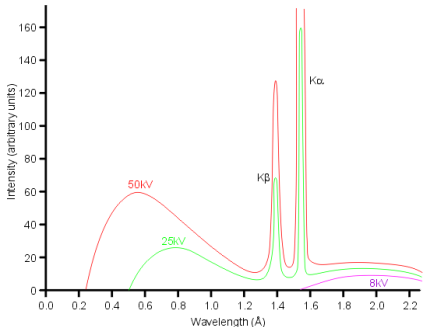

Figure 3.1. X-ray spectrum of Cu anode.

appear in the spectrum. These characteristic lines are the result of K, L, M, etc. spectral line emissions of the anode material. The K series lines $K\alpha_1, K\alpha_2, K\beta_1$ (see Figure 3.1 for copper) have the highest intensity and are most suitable for structural studies [32], since their wavelengths are compatible to typical lattice parameters of crystalline solids. Once the characteristic X-rays are produced, the beam undergoes a series of optical treatments e.g. Söller collimators and the useful wavelengths are filtered out by material filters (Fe, Ni, etc.) that are picked to absorb bremsstrahlung and other characteristic lines.

After that the beam is incident at the surface of the material to be studied, where it gets partially absorbed and scattered. Waves scattered elastically from crystalline solids produce diffraction patterns described by Bragg's Law. Figure 3.2 shows a pair of coherent X-rays scattering off two lattice planes separated by distance d_{hkl}. The ray reflecting off

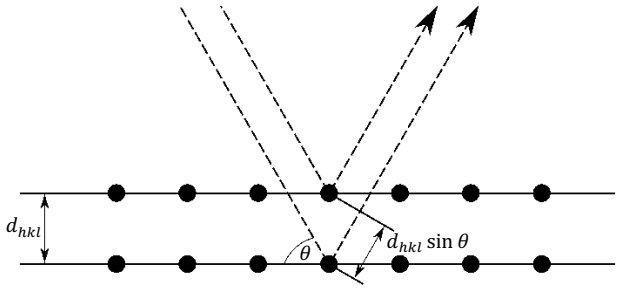

Figure 3.2. Illustration of Bragg's Law.

the bottom plane travels a longer distance to the detector, thus arriving with a different phase $\Delta\phi = 2d_{hkl} \sin \theta$.

If the phase difference is an integer multiple of the wavelength of radiation, the two rays will interfere constructively, creating an intensity peak. Therefore, by rotating the detector and finding the peaks one can extract the distance between various (hkl) planes of the material. In the cubic case,

$$2d_{hkl}\sin\theta = n\lambda \tag{3.1}$$

where d_{hkl} – distance between (hkl) planes, θ – angle of scattering, λ – wavelength of radiation, n – an integer, representing the order of the diffraction. When the lattice parameters and symmetry group of the material are known, formula (3.1) or crystallographic simulation software allow for easy identification of Bragg peaks determined experimentally.

3.1.2 Equipment

All X-ray diffraction studies presented in this work were performed on Phillips X'pert Diffractometer. The diffractometer is equipped with a copper ($\lambda_{K\alpha_1} = 1.54056$Å) X-ray tube operating in line and point configurations, incident ray optics, $\theta - 2\theta$ goniometer with a sample stage, reflected ray optics, and a Xenon proportional counter detector. A detailed drawing of the goniometer is shown in Figure 3.4.

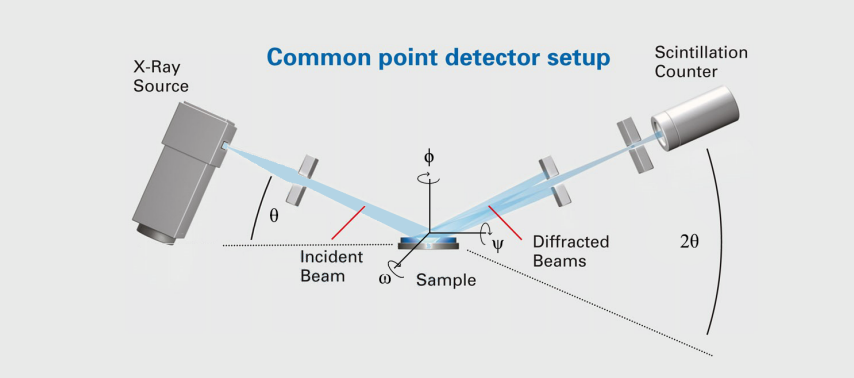

Figure 3.3. Schematic of the $\theta - 2\theta$ goniometer with Euler angles labeled.

In addition to the 2θ angle traversed by the detector, the sample stage rotates through angles ω, ϕ, and ψ, thus completing the set of Eulerian angles. Here, ω is the tilt of the sample around the y-axis (the axis perpendicular to the beam in the plane of the sample), ϕ is the rotation of the sample around the z-axis (axis normal to the plane of the

sample), ψ is the tilt of the sample around the x-axis (the axis parallel to the beam in the plane of the sample).

3.1.3 Crystal Orientation

Precise orientation of single-crystalline samples plays a crucial role in measurements focused on anisotropic transport. In addition, transport measurements of magnetic materials are very sensitive to exact alignment of external magnetic field with a particular crystallographic direction of the sample. X-ray diffraction allows for a precise method of sample orientation in virtually any crystallographic direction. If the desired direction is in the plane of the sample, the orientation is carried out by finding the three goniometer angles corresponding to the Bragg peak of the direction that "covers" the sought after in-plane direction and projecting that out-of-plane direction onto the plane. If the desired direction is out-of-plane of the sample, the sample needs to be polished or cut to create a flat surface that is parallel to the desired direction.

3.1.4 Characterization Techniques

In experimental science, consistency and reproducibility are among the top concerns, so it is crucial that every sample measured is properly characterized to account for variations between samples. X-ray diffraction offers a variety of characterization techniques that reveal information about the crystalline quality of the sample, non-stoichiometry, internal strains, twinning, and defects, crystallographic phases, thickness, grain size, and texture in the case of thin films.

Determination of Lattice Parameters.

As was discussed in the previous chapter, Bragg's Law can be used to obtain distances between lattice plains (hkl). Combined with information about the geometry of the crystal system [32], this can be used to calculate lattice parameters of the solid. Experimentally, one needs to find 2θ angles of a series of Bragg peaks reflected off an (hkl) plane. In general, the calculation is challenging, since the order of the reflection is *a priori* not known, but the result can be achieved with structure refinement procedures. Most of the times when working with crystals, lattice parameters of the material are already known, but may vary between specimens. These variations can influence physical properties like transport measurements, thus, we employ an advanced procedure based on high angle extrapolation to minimize experimental error in lattice parameter determination. In the case of cubic crystals, the extrapolation function for the interplanar distance $d_{hkl}(\theta)$ has the following dependence on the scattering angle θ:

$$d_{hkl}(\theta) = a_0 + a_0 K \left(\frac{cos^2(\theta)}{\sin(\theta)} + \frac{cos^2(\theta)}{\theta} \right) \tag{3.2}$$

where a_0 is the true value of the lattice parameter and K is a constant [32].

Crystalline Quality.

Transport measurements in single crystalline samples are very sensitive to presence of various crystalline defects like point defects, small angle domain walls, twinning, etc. Therefore, a thorough verification of best crystalline quality is required. Pole figure scans allow to identify the presence of low angle domain walls and unwanted domains in the bulk of the crystal. To construct a pole figure, 2θ is set to a value corresponding to that of a high intensity Bragg peak, and then the sample is rotated through angles ϕ and ψ. The resulting pole figure should match the symmetry of the lattice, and extra peaks at unexpected angles

signal the presence of other domains. Another XRD technique that reveals a lot of information about lattice defects like dislocations, misorientations, and inhomogeneity is the rocking curve scan, which measures the width of the Bragg peak in the ω plane. The rocking curve scan is performed by holding the 2θ fixed and scanning the ω angle through the Bragg peak.

X-ray Reflectivity (XRR)

In X-ray reflectivity an X-ray beam is incident on the surface of a thin film at a very small angle (grazing incidence). Incident beam creates specular reflections that are measured by the detector. The resulting oscillatory pattern contains a lot of information about the characteristics of the film like its thickness, critical angle, roughness, density, grain size, etc. Figure 3.7(a) shows a typical XRR pattern. Film thickness t can be roughly estimated as

$$t = \frac{\lambda}{2\Delta\theta} \tag{3.3}$$

where $\Delta\theta$ is the width of the fringe in radians, λ – the wavelength of X-rays.

A more precise method is to use linear regression based on

$$q^2 = \frac{2\pi}{t}(m + \Delta m)^2 \tag{3.4}$$

where q and m are, respectively, the wavevector the order of maxima or minima of the oscillatory pattern, and $\Delta m = 0.5$, if the density of the film is smaller than the density of the substrate (Figure 3.4(b)). Figure 3.4(c) shows the plot of Pt film thickness as a function of deposition times used to calibrate deposition rate of 0.593 nm/s at a fixed target current $I_{tar} = 41\ mA$ and argon pressure $p_{Ar} = 0.08\ mbar$.

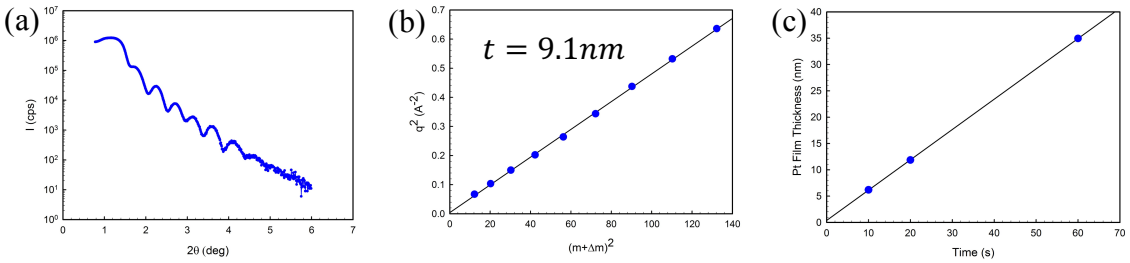

Figure 3.4. (a) XRR pattern of a 9nm Pt film on Si substrate. (b) Film thickness calculation based on extrapolation formula (Eq. 3.4). (c) Film thickness vs. deposition time.

3.2 Sample Preparation

Steady state thermal conductivity and longitudinal spin Seebeck measurements produce best results, when the measured sample has a regular parallelepipedal shape with faces oriented in specific crystallographic directions. Single crystals oriented by XRD undergo a series of cutting, polishing, and orientation verification steps before a desired geometry is obtained. Materials with high thermal conductivity require the dimension of the sample parallel to the heat flow to be big enough to result in precise measurements of the temperature gradient and the magnitude of spin Seebeck voltage depends on the width perpendicular to external magnetic field, so one of the challenges of sample preparation is to evaluate the shape and orientation of the crystal and make a cut that would maximize those dimensions. Cuts are made with a wire saw shown in Figure 3.5a and the orientation of the cut plane is reconfirmed by XRD. In situations when the cut is a few degrees off from the desired orientation, the cut surface is polished with abrasive grinding papers on a lapping machine (Figure 3.5b) at an angle to eliminate the misalignment. The procedure outlined above is repeated multiple times until the sample is shaped into a parallelepiped.

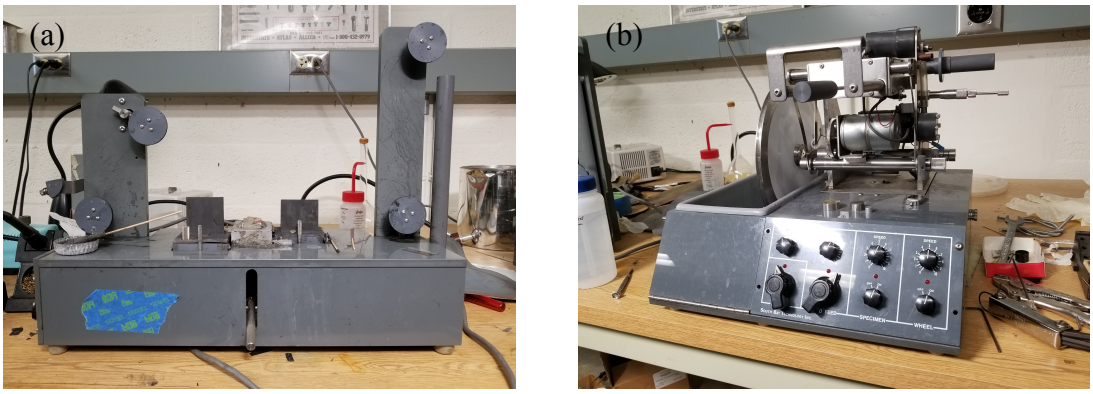

Figure 3.5. Equipment used in sample preparation. (a) Wire saw. (b) Lapping machine.

3.3 Thin Film Preparation

Spin Seebeck measurements rely on the ability of metals with strong spin-orbit coupling (Pt, Ta, W) to convert spin currents to measurable voltages via the inverse spin Hall effect. Typically, the diffusion length of spin currents into the metal is on the order of a few nanometers [33], [34], therefore a thin film of one of listed materials constitutes an excellent spin current detector. In spin Seebeck experiments described in this work, platinum films with thickness 8-10 nm have been deposited by DC magnetron sputtering onto the face of the sample perpendicular to the direction of the heat flow. The outome of a spin Seebeck experiment strongly depends on the quality of the thin film and treatment of the surface it's deposited on [35], [36], so the following sections will outline the procedure used to prepare the surface before the deposition and methods employed to characterize the deposited film.

3.3.1 Surface Treatment

Each sample described in this study underwent the three step surface preparation process. First, the narrow rectangular face of the sample was polished with abrasive grinding papers of decreasing roughness on a lapping machine: 1) Silicon Carbide, 25μm;

2) Silicon Carbide, 5µm; 3) Silicon Carbide, 1µm; 4) Aluminium Oxide, 0.3µm. Due to the small dimesions of the sample, it was attached to a copper block with crystalbond, so that the polished surface is flush with the copper to minimize the stress on the sample during polishing. After that the entire sample was cleaned in an ultrasonic bath and mounted on a custom sample holder with crystal bond. Then the surface was treated with the Piranha solution (3:1 mixture of concentrated sulfuric acid and 30% hydrogen peroxide) by dipping the polished end of the sample in a Petri dish with solution to remove remaining organic residue. Over the span of multiple experiments described in this study, treatment times have been reduced from 60s to 5s as a result of an observation of a strong etching of the sample surface. After the Piranha treatment the sample was rinsed with deionized water and dried with air, followed by an immediate transfer to the deposition chamber.

3.3.2 Magnetron Sputtering

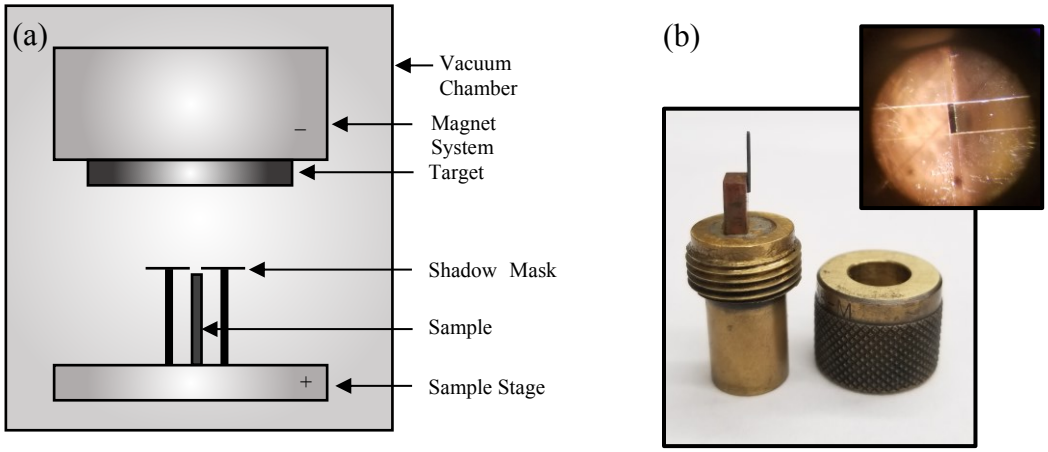

Figure 3.6. (a) Schematic of the sputtering chamber. (b) Sample holder and shadow mask.

Magnetron sputtering is a physical vapor deposition process primarily used in fabrication of thin films. In the proces, the sputterng gass is ionized, and poitively charged ions are accelerated by the electric field towards the cathode, bombarding and ejecting

atoms from the target. Ejected atoms then diffuse away from the target and condense on the sample (see Figure 3.6a).

A Cressington 108 sputter coater with platinum target installed was used to deposit films on all Cu_2OSeO_3 samples in this study. Ultra high purity argon was used as the sputtering gas and the vacuum chamber was pumped with a diffusion pump. Deposition rates were calibrated by performing reflectivity thickness measurements (see Section 3.1.4) on a series of Pt/Si samples with increasing deposition times. All other deposition parameters like the distance from the target, argon pressure, and target current were not varied.

The thin film deposition procedure consisted of the following steps. Once the etched and dried sample was transferred into the deposition chamber, a shadow mask was installed on top of the sample holder cap. The shadow mask cut from microscope slide cover was designed to expose the narrow polished face of the sample while keeping the rest of the sample masked. In addidion, the shadow mask was aligned flush with the face of the sample to guarantee complete and uniform coverage (Figure 3.6b). After that the vacuum chamber was sealed and pumped with a diffusion pump to the base pressure of 1×10^{-5} mbar and flushed with argon three times. The argon pressure in the chamber was set to $P_{Ar} = 1 \times 10^{-2}$ mbar and the platimun was deposited for 80 seconds at the target current of 16mA.

Four thin (0.001" diam.) gold are attached at the two ends of the platinum film with silver epoxy (Epo-Tek® EE165) and the sample is annealed in a 250°C furnace for 15 mins to cure the epoxy and improve contact resistance.

3.3.2 Film Characterization

Thin films are characterized with XRR to determine their thickness, roughness, and grain size. Other characterization thechniques involve low-temperature measurements of resistivity, magnetoresistance, and Hall coefficient (see Section 6.2).

3.4 Transport Measurements

Our lab specializes on low temperature transport measurements and a number of different measurements were performed in the scope of this work. This section will discuss the equipment, experimental techniques, and setups used for the measurements.

3.4.1 Thermometers and Thermocouples

Ruthenium Oxide Thermometers

Ruthenium oxide bare chip thermometers are exellent temperature sensors for temperatures below 20K. Their charasteristic feature is that the resistance of the amorphous ruthenium oxide film increases very fast with decreasing temperature, so a small change in the temperature of the film results in a big change in its resistance, allowing for a very precise measurement of absolute temperature.. The resistance of the film is measured using the 4-wire configuration, and then converted to absolute temperaure using T(R) calibration curves shown in Figure 3.7. Bare chip sensors come uncalibrated, so they need to be calibrated against a standard precalibrated thermometer in a separate experiment to obtain T(R) data.

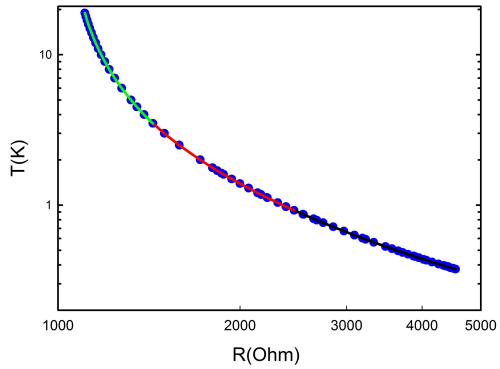

Figure 3.7. Typical $T(R)$ calibration data of a bare-chip Ruthenium oxide thermometer (circles). Fits based on Eq. 3.5 (lines).

The data are fit with the piece-wise model and non-linear regression is used to determine fit coefficients.

$$T(R) = \begin{cases} A_1\left(\dfrac{B_1}{(T+C_1)^{D_1}}\right), & when\ 0K < T \leq 1K \\ A_2\left(\dfrac{B_2}{(T+C_2)^{D_2}}\right), & when\ 1K < T \leq 3.5K \\ A_2 + B_2 T^2 Ln(T), & when\ 3.5K \leq T \end{cases} \tag{3.5}$$

Thermocouples

A thermocouple is a temperature sensor that consists of two wires made of metals with very different Seebeck coefficients (S_1 and S_2), that are welded together at one end to form a junction. Whenever there is a temperature gradient ΔT between the junction and the ends of the thermocouple, the difference in the Seebeck coefficients $S_1 - S_2$ of the two metals produces a voltage V across the two ends. If the absolute temperature of the ends T_{ref} is known, the temperature of the junction $T_{junction}$ can be calculated using the formula

$$T_{junction} = T_{ref} + \frac{V}{S_1 - S_2}. \tag{3.6}$$

Type E (chromel-constantan) thermocouples are very useful in low temperature measurements, because of their hight voltage output at cryogenic temperatures.

3.4.2 Resistivity and Magnetoresistance

The DC resitance measurement that utilizes the 4-wire setup is the most commonly used method often empoleyd to measure resistivities of bulk single crystals, thin films, or resistances of various resistive devices like thermometers and heaters. This method has a number of advantages over the 2-wire setup: current reversal accounts for various offsets, resistances of the leads and contact resistances are ignored. Leads A are designed to create a uniform current density throughout the specimen. The current I is suppled by a Keithley 220 programmable current source that can output currents in the range between 100nA and 1A. Leads B are used to measure the voltage drop V using a Keithley 2182A, able to detect voltages between 3V and 10nV. These instruments then can be used to measure resistances in the range from 10nΩ to 30kΩ. The resistivity of the sample can be calculated using

$$\rho = \frac{V}{I}\frac{A}{l} \tag{3.7}$$

where V is the voltage across leads B, I is the current through leads A, A is the crossectional area of the specimen, and l is the distance between leads B. The biggest challenge of this method is to ensure that the current density between leads A is uniform, that is why it is partucularly important to create contacts of the right shape. The contacts can be hand pained on with a conductive silver epoxy, or magnetron sputtering can be used to deposit Au or Pt contacs through a shadow mask (see Section 3.3.2). In this work the technique was used multiple times in the following situations: resistance of ruthenium oxide thermometers was measured and converted to absolute temperature, resistance of chip heaters was used to calculate the power output of the heater, resistance of the platinum film

was measured as a function of temperature and magnetic field to investigate the effects of proximity magnetization on spin Seebeck effect (more in Section 6.2).

3.4.3 Thermal Conductivity

There is a number of experimantal techniques that can be used to measure thermal conductivity κ, but the most advantageous method for measuring thermal conductivity of single crystals with heat flow in a particular crystallographic direction is the steady state method. The schematic of the measurement setup is shown in Figure 3.8.

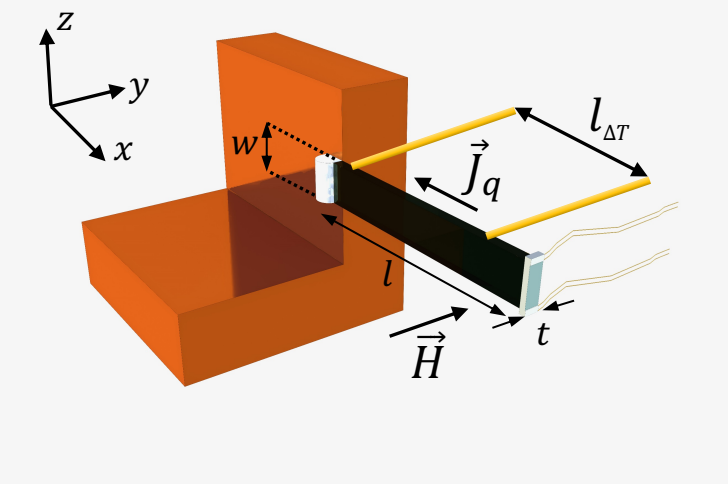

Figure 3.8. Schematic of the thermal conductivity measurement setup.

To achieve the desired configuration, the first step is to cut a rod-like specimen with dimensions $l \times w \times t$ out of an oriented single crystal, so that the length of the rod is parallel to the desired crystallographic direction, and the crossection is rectangular and uniform (to guarantee a uniform tempertature gradient required for this method). Then the sample is attached to a thermally conducting heat sink (typically OFHC copper) with an epoxy appropriate for the measurement. The common thermally conducting epoxies are silver paint, GE varnish, stycast, E20 silver epoxy, etc, and a number of factors need to be considered when choosing the right one, including the temperature range of the

measurement, electrical conductivity, ability to adhere to the surface of the crystal, grain size/uniformity, and mechanical strength. The third step is to attach the resistive chip heater (look up the manifacturer) to the cantilever end of the sample, thus creating a heat flow $\vec{J}_q$ through the sample from the heater to the sink. There are a few options regarding what temperature measuring devices to use to measure the temperature gradient and the average temperature of the sample, depending on the desired temperature range. At low temperatures, 0.1K ≤ T ≤ 20K, Ruthenium Oxide chip thermometers provide the best temperature resolution, in addition, their low magnetoresistance makes them really usefull for field dependent measurements. For all other temperature ranges, a combination of a differential thermocouple and an average thermocouple of type E or K can be used. The junctions of the differential thermocouple (or RuO_2 thermometers via thick gold wires) are attached to the sample at a maximum separation, while the average thermocouple junction is placed in between the two. In the steady state method, thermal conductivity is calculated by

$$\kappa(T_{avg}) = \frac{V_{htr} I_{htr}}{\Delta T} \frac{l_{\Delta T}}{A} \tag{3.8}$$

where V_{htr} is the heater voltage, I_{htr} is the heater current, ΔT is the temperature difference between the points separated by length $l_{\Delta T}$, and $A = wt$ is the cross-sectional area of the sample. The current through the heater I_{htr} is supplied by the Keithley 220 programmable current source, the voltage V_{htr} is measured with the Keithley 2182A nanovoltmeter in a four wire setup. In the case of resistive thermometers, the four wire method is used to calculate the resistance of each thermomter, which is later converted to the absolute themperature using T(R) calibration curves (see 3.4.1). The temperature difference ΔT and the average temperature T_{avg} are then caluculated by finding the difference and the average

of two thermometer readings, respectively. In the case of thermocouples, the two voltages V_{diff} and V_{lag} of the differential and the average thermocouples, respectively, are measured by a nanovoltmeter and then converted to the temperature difference and average temperature by the method described in 3.4.1). In some situations it is possible to have a non-zero temperature gradient along the sample even when the heater is off. In order to account for that in the calculation of thermal conducivity, a separate measurement of zero heater power (heater off) temperature gradients needs to be performed throughout the temperature range, giving a function $\Delta T_{0htr}(T_{avg})$. Then the true thermal conductivity can be calculated by

$$\kappa(T_{avg}) = \frac{V_{htr} I_{htr}}{\Delta T - \Delta T_{0htr}(T_{avg})} \frac{l_{\Delta T}}{A}. \tag{3.9}$$

3.4.4 Spin Seebeck Effect

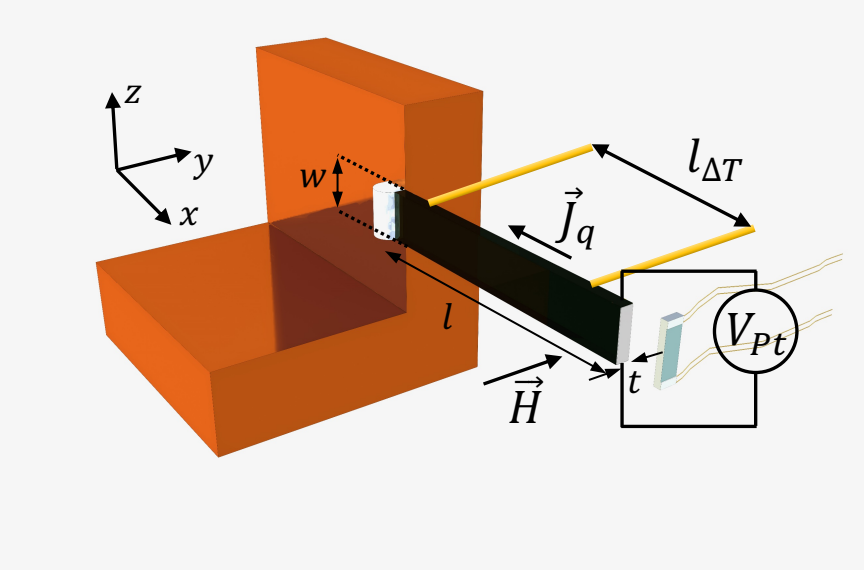

Figure 3.9. Schematic of the spin Seebeck effect measurement setup.

Spin Seebeck effect in Cu_2OSeO_3 was measured in the longitudinal configuration presented in Figure 3.9. This setup is similar to the one for thermal conductivity measurements presented in Section 3.4.3 except for the addition of an 8-10 nm platinum (Pt) thin film on the face perpendicular to the heat flow direction. In order to maximize the LSSE signal, several considerations regarding sample geometry need to be taken into account.

First, samples need to be of parallelepipedal geometry that maximizes the length l along the heat flow to produce the maximum temperature difference ΔT_x, as LSSE voltage is directly proportional to the temperature gradient. Secondly, since LSSE voltage originates as an electric field of inverse spin Hall effect integrated along the width w of the sample, the width needs to be maximized as well. The second condition competes with the first, since the geometric factor $g = \frac{l}{wt}$ ultimately determines the magnitude of the temperature difference. Experimentally, it is beneficial to have the biggest possible geometric factors for materials with high thermal conductivity to avoid temperature differences at the limit of thermometer sensitivity. For majority of the samples, the length is determined by the size of the bulk single crystal it is cut from, thus reducing thickness t of the sample while keeping w relatively large is the strategy that maximizes the LLSE signal. With the heat current $\vec{J}_q$ in the $\hat{x}$ direction and magnetic field $\vec{H}$ in the $\hat{y}$ direction, the inverse spin Hall voltage in the platinum strip is expected to be in the $\hat{z}$ direction, thus four 0.001-inch diam. wires are attached at the two ends of the strip.

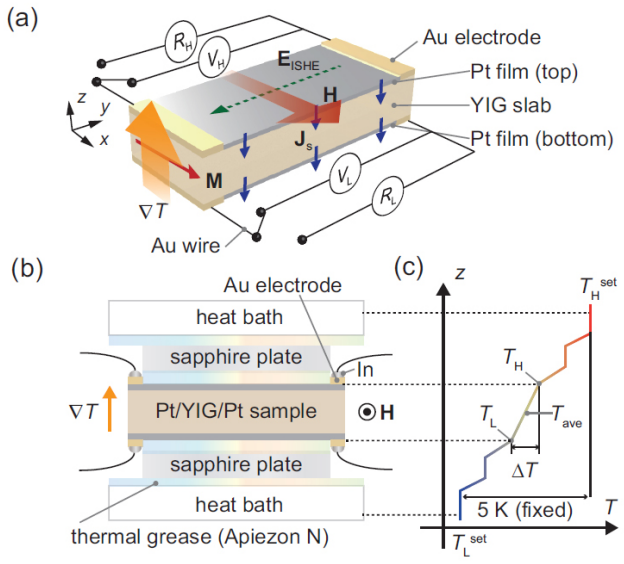

Figure 3.10 (from Ref. [38]). (a) Schematic illustration of the Pt/YIG/Pt sample. (b) Experimental configuration for applying ∇T. (c) A schematic plot of temperature profile along the z direction.

The setup described is distinguished from the measurement configurations typically used in the studies of LSSE in bulk YIG (Figure 3.10a) but offers certain advantages. Since thermal conductivity of YIG is much smaller, wide, short samples are sandwiched between two heat baths with sapphire plates on the two sides to produce uniform heat flow. The temperature of the two sapphire plates is directly measured and the difference is taken to be equal to the temperature difference in the YIG slab. Figure 3.10c shows that this approach is prone to erroneous measurements of the temperature gradient as the actual temperature profile across the stack is rather complicated due to a finite thermal resistance of the contacts between the YIG and sapphire plates. Instead, authors of Ref. [37], [38] propose to use platinum films deposited on the two ends as thermometers by calibrating the temperature dependence of their resistance.

This method improves the accuracy of the temperature gradient measurement at T > 20K but gives poor results at low temperatures as platinum resistance becomes weakly

temperature dependent in the residual resistance regime. Also, this method complicates the analysis of magnetic field dependence as separate calibrations over the entire temperature range need to be performed to determine the film resistance as a function of field and temperature. Therefore, the method described in this section has definite advantages as it affords directly measured temperature gradients with sensitive, calibrated (in field) thermometers.

3.5 Data Acquisition

3.5.1 Equipment

A wide range of equipement was used to enable fast and reliable measurements and recording of the data in the experiments described in this work. A fully automated setup of Keithley® 224 programmable current sources, model 182 and 2182 nanovoltmeters, a model 705 switch sytem, Lakeshore® 335 temperature controllers, and a model 625 superconducting magnet power supply, communicating via GPIB interface was used for to perform measurements and transfer the results to a PC.

All low-temperature measurements were performed in the Cryo Industries of America, Inc model He3-PRO® dipper probe equipped with a 5T superconducting magnet placed in a dewar with liquid helium. The probe's cooling system is capable of maintaining a base temperature of 300 mK for extended periods of time. The key components of the cooling system − charcoal chamber, condensation pot (He^4 pot), and He^3 pot − are shown in Figure 3.11.

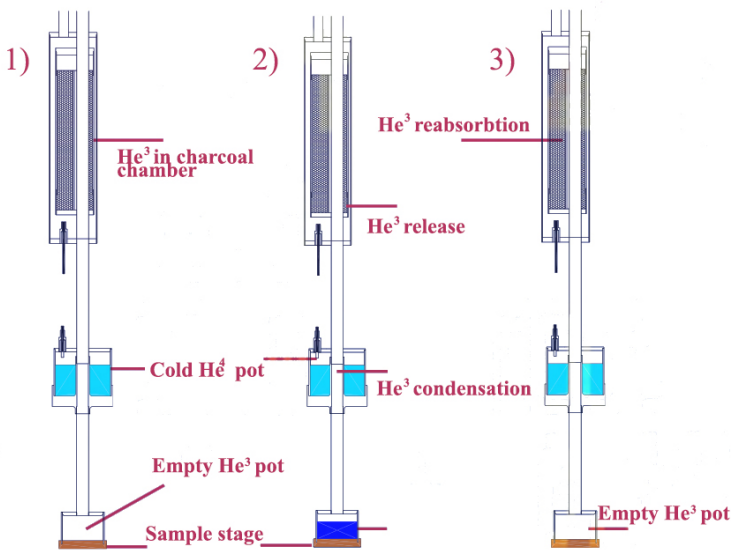

Figure 3.11 (adapted from [39]). Components of He^3 probe cooling system and steps of operation.

The principle of operation is based on thermodynamic cycling of He^3 gas that occurs in the following steps:

1) The charcoal chamber is heated and the stored He^3 gas is released
2) He^3 gas passes though the condensation pot at temperatures below 1.7K and condenses in the He^3 pot, then charcoal heater is switched off and liquid He^3 provides cooling power for the sample stage
3) Heat loads on the sample stage evaporate liquid He^3 that is physisorbed one the charcoal surfaces.

Sample vacuum space is diffusion pumped and backed by an Edwards® Model 1.5 dual stage rotary pump. Pumping on the charcoal chamber and He4 pot is done with an Edwards® Model 5 dual stage rotary pump.

3.5.2 Software

The data acquisition was performed using an automated LabView routine designed to communicate with digital equipment, coordinate a measurement sequence, and record data. Additional features were used to monitor temperature changes of stage thermometers and condenser pot thermometers to guarantee excellent temperature stability over the course of multiple-hour magnetic field sweeps at fixed temperature setpoints.

Chapter 4. Cu_2OSeO_3 − Overview of Properties

In this chapter we will go over the physical properties of Cu_2OSeO_3 and review relevant experimental and theoretical work published about this material. We will also develop an understanding of the key properties of Cu_2OSeO_3 that motivated the study of thermal conductivity and spin Seebeck effect in this material. In addition, we will draw comparisons with YIG and discuss the avenues the study of Cu_2OSeO_3 can lead to, establishing the potential contributions to the field of spin caloritonics it can bring.

4.1 Structure

The first studies of CuO-SeO_2 compounds were done by G. Meunier and M. Bertaud in 1976 [40]. X-ray analysis of single crystals and powder samples was used to determine the cubic lattice system and the space group $P2_13$ of Cu_2OSeO_3. A 1986 study by H. Effenberger and F. Pertlik determined the crystal structure, atomic positions, and the lengths of Cu-O and Se-O bonds [41]. Bos *et. al.* [42] grew single crystals of Cu_2OSeO_3 by the chemical vapor transport (CVT) method, refined the crystal structure via XRD and neutron powder diffraction, and measured thermal expansion, magnetization, ac susceptibility, and dielectric constant over a wide temperature range with the focus around the Curie temperature $T_c \approx 58K$. Further analysis of the structure revealed that, the noncentrosymmetric $P2_13$ space group implies Cu ions form a distorted, three-dimensional pyrochlore lattice of corner sharing tetrahedra (Figure 4.1a). Within the tetrahedra there are two inequivalent sites of Cu^{2+} with different oxygen coordination (Cu_1 and Cu_2). Cu_1 ions are surrounded by square pyramids of oxygen ligands, while Cu_1 ions are surrounded by trigonal bipyramids. Magnetization was found to saturate at a value of $0.5\mu_B/Cu^{2+}$ which

supported the collinear ferrimagnetic alignment of copper spins within the tetrahedra with three (Cu_2) pointing in the same direction and one (Cu_1) antiparallel (Figure 4.1b). The absence of spontaneous lattice strain, magnetostructural coupling, as well as anomalous behavior of dielectric constant and magnetocapacitance suggested a unique nature of magnetoelectric coupling.

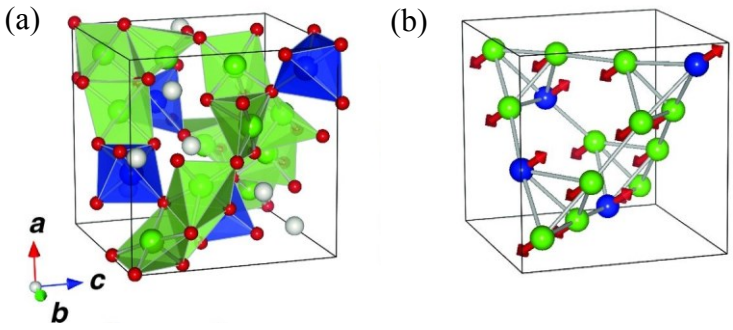

Figure 4.1 (from Ref. [48]). (a) Crystal structure of Cu_2OSeO_3. Cu_1 in blue, Cu_2 in green, O in red, Se in grey. (b) Orientation of Cu^{2+} spins.

Belesi *et al.* reported a nuclear magnetic resonance (NMR) study of ^{77}Se nuclear spins in Cu_2OSeO_3 [43]. The NMR effectively probes the electronic moments of Cu^{2+} atoms through the transferred hyperfine and magnetic dipolar interactions with ^{77}Se nuclear spins. The study confirmed the ferrimagnetic ordering of Cu^{2+} spins within the tetrahedra and identified anomalous behavior around T_c of spectral lines associated with phonon modes responsible for the magnetoelectric effect.

4.2 Magnetism

Metallic B20 alloys share the noncentrosymmeric space group $P2_13$ with Cu_2OSeO_3 and exhibit chiral helimagnetic order. These B20 compounds were also shown to host topological spin vortices − skyrmions. Structural similarities of Cu_2OSeO_3 with transition metal alloys with B20 structure, like MnSi [44], [45], $Fe_{1-x}Co_xSi$ [46], and FeGe

[47] motivated a series of small angle neutron scattering (SANS) and Lorentz TEM imaging studies of its magnetic structure. The studies [48], [49],[51] revealed that below the transition temperature, competing $\vec{S}_i \cdot \vec{S}_j$-like ferromagnetic exchange and $\vec{S}_i \times \vec{S}_j$-like Dzyaloshinskii-Moriya (DM) interactions (favoring parallel and perpendicular spin alignment, respectively) result in helimagnetic ordering of S=1 tetrahedra below T_c and are also responsible for the appearance of the skyrmion phase near T_c.

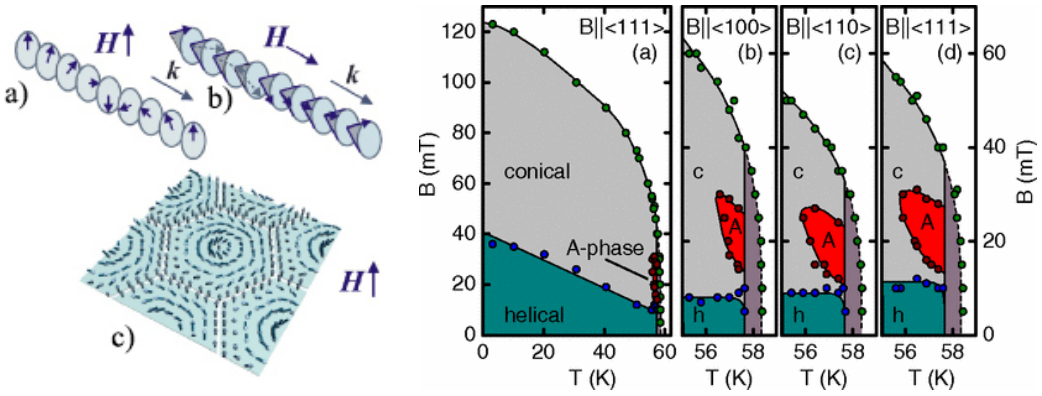

Figure 4.2. (a-c) (from [52]) Spin textures in the helimagnetic, conical, and skyrmion phases, respectively. (d) (from Ref. [51]) Magnetic phase diagram.

Figure 4.2a shows an illustration of the spin configuration in the helical phase; here the total spins of the tetrahedra rotate in the plane perpendicular to the propagation vector $k = 2\pi/\lambda_h$, that is parallel to the <100> crystallographic directions and $\lambda_h \approx 616 \pm 45$ Å is the modulation wavelength. This particular direction of the propagation vector is caused by the magnetic anisotropy, while the high symmetry of the cubic lattice results in three coexisting <100> domains as confirmed by SANS. As the external magnetic field increases, Cu_2OSeO_3 undergoes a second order phase transition at the first critical field H_{c1} from the helical into the conical phase, where the spins begin to rotate on the surface of a cone and the propagation vectors align with the direction of the field forming a single domain (Figure 4.2b). Above the second critical field H_{c2} the spins of the tetrahedra align

parallel with the magnetic field and the material is in the field-polarized (or collinear) phase, while maintaining the ferrimagnetic ordering within the tetrahedra at least up to 14T [43]. The phase diagram for the magnetic phases described so far is presented in Figure 4.2d.

Recently, Qian *et al.* [53], Chacon *et al.* [54], and Halder *et al.* [55] experimentally observed two new spin phases of Cu_2OSeO_3: a low-temperature skyrmion phase and a so-called tilted conical phase. Both new phases occur exclusively when the magnetic field direction is along the [100] crystallographic direction, favored by cubic anisotropy. The tilted conical phase (TC) is characterized by a tilt of the direction of conical modulation away from the field direction toward <111> directions, resulting in a multidomain phase with temperature dependent tilt angle. The phase occurs at magnetic fields near $0.6 \cdot H_{c2}$ and is stabilized by competing magnetic anisotropies.

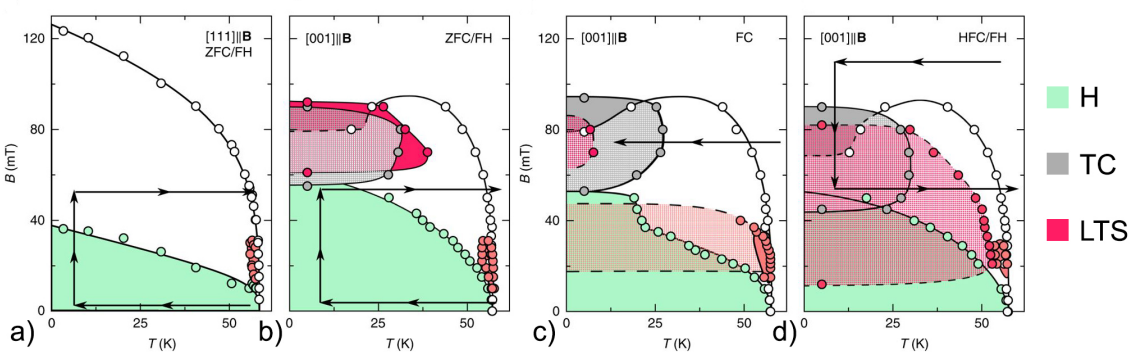

Figure 4.3 (from Ref. [54]). (a) Magnetic phase diagram observed for ZFC/FH and field parallel to ⟨111⟩. (b-d) Magnetic phase diagrams observed for ZFC/FH, FC, and HFC/FH, respectively, for field parallel to ⟨100⟩. Hatched shading represents coexistence of skyrmion and TC phases.

Chacon *et al.* argued that the observed ring of scattering intensity that is perpendicular to the field in parts of the tilted conical phase can be attributed to the presence of a triangular skyrmion lattice (LTS). Additionally, they concluded that the transition from the conical phase to the TC is second order, while the transition from FP to TC is first

order. All transitions to LTS are strongly first order and are additionally protected by topology. Figure 4.3 shows the magnetic phase diagram obtained from SANS data for three temperature vs field protocols: zero-field-cooled/field-heated (ZFC/FH), field-cooled (FC) and high-field-cooled/field-heated (HFC/FH).

4.3 Heat Capacity

Recently, magnetic field dependence of specific heat of Cu_2OseO_3 had been reported by Halder *et al.* [55]. These data turn out to be very useful in the analysis of magnetic dependence of thermal conductivity presented in Section 5.3. Figure 4.4 shows the change in specific heat $\Delta C = C(B) - C(H = 0)$ at T = 2 K as a function of magnetic field for three principal crystallographic directions.

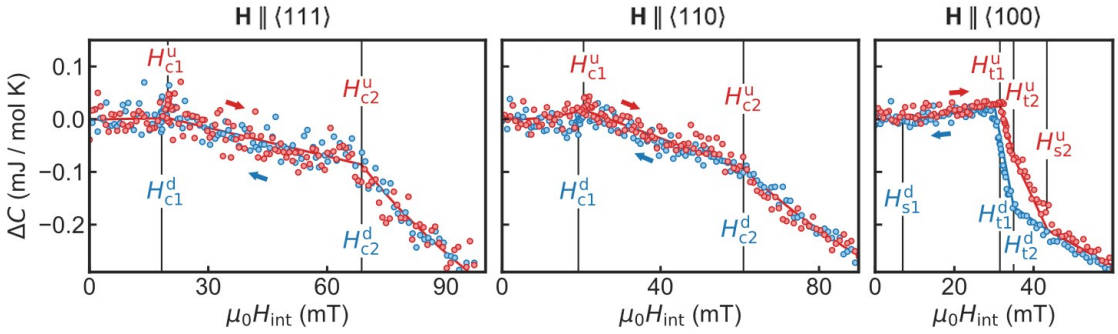

Figure 4.4 (from Ref. [55]). Field dependence of specific heat at 2 K for three principal directions. Red (blue) circles correspond to increasing (decreasing) field.

4.4 Crystal Growth

The bulk single crystal specimens used in this study were prepared by our collaborators (group of Tyrel McQueen at Johns Hopkins University) using the seeded chemical vapor transport method described in [58].

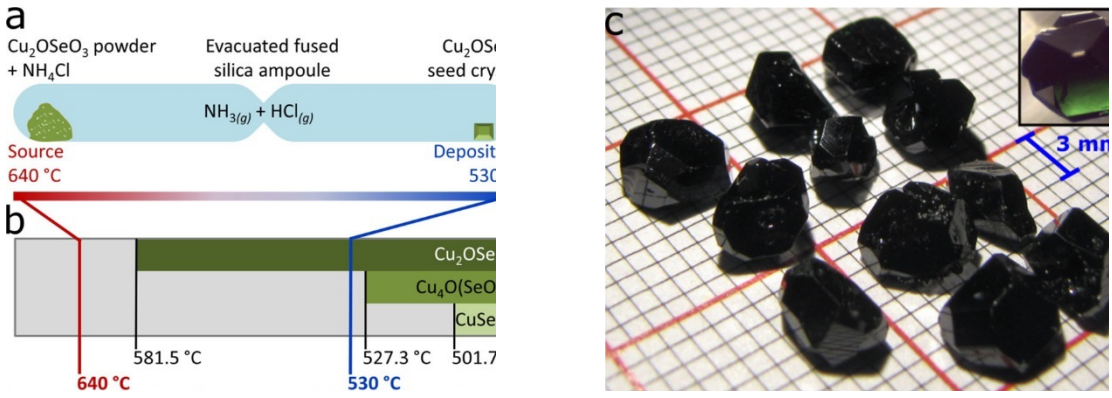

Figure 4.5 (from Ref. [58]). a) Seeded CVT setup. b) Temperature gradient chosen to sigle out the growth of Cu_2OSeO_3. c) Large Cu_2OSeO_3 crystals grown by the seeded CVT method.

First, polycrystalline Cu_2OSeO_3 is synthesized by a direct solid-state reaction of CuO and SeO_2. Ground up precursors (in a 2:1 molar ratio) are sealed in an evacuated fused silica ampule and the temperature is ramped to 600°C at a rate of 100°C/hr. and held at 600°C for 12 hours, followed by a quench of the tube in water. To grow single crystals Cu_2OSeO_3 powder is sealed in a fused silica ampule with 0.4 mg/cm^3 NH_4Cl. The tube is then positioned between the first two zones of a three-zone tube furnace. The source zone is ramped to 640°C and the deposition zone – to 530°C as depicted in Figures 4.5 a, b and the temperature gradient is maintained for 6 weeks. The obtained small single crystal specimens are then used in the seeded CVT growth, producing large, olive green Cu_2OSeO_3 crystals shown in Figure 4.5c. Powder XRD was used to confirm phase purity and back-reflection X-ray Laue diffraction was utilized to identify crystal faces and verify crystalline quality.

Chapter 5. Thermal Conductivity of Cu_2OSeO_3

We will start this chapter by going over the considerations that drew our attention to Cu_2OSeO_3 and motivated our study of its thermal conductivity. Then the essential results of thermal conductivity studies, published by our group [59], [60], will be presented.

5.1 Skyrmion Thermal Hall Effect

Originally Cu_2OSeO_3 drew our attention because of the possibility of an observation of skyrmion thermal Hall effect. Recent theoretical work [61], [62] described skyrmion dynamics in the presence of a temperature gradient. These studies found that in addition to the usual Brownian drift of skyrmions opposite to the temperature gradient, there is an overwhelming flow in the opposite direction caused by negative spin transfer torques on skyrmions caused by the magnon current induced by the temperature gradient. The overall drift is in the direction along the temperature gradient (cold to hot), contrary to the intuitive diffusion direction of other carriers and quasiparticles. In addition, the theory suggests that the DM interaction in the presence of an external magnetic field results in skyrmion drift transverse to the temperature gradient. The heat current produced by this motion of skyrmions creates a transverse temperature gradient.

The first experiments done by our group focused on measuring the proposed skyrmion thermal Hall temperature gradient. The measurement setup, displayed in Figure 5.1, was similar to the thermal conductivity setup described in Chapter 3 with type E differential thermocouples measuring the longitudinal and transverse temperature differences.

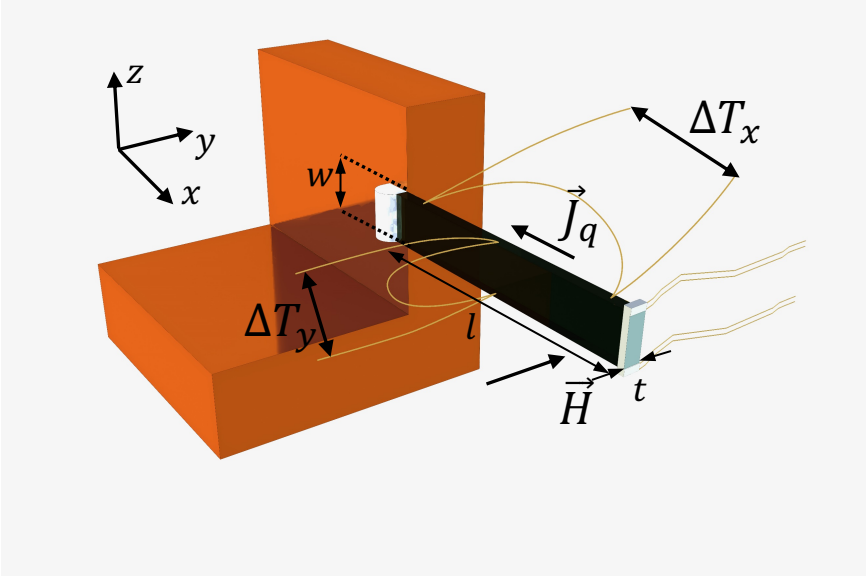

Figure 5.1. Skyrmion thermal Hall effect measurement setup.

The sample with length l parallel to the [111] crystallographic direction and width w perpendicular to $[1\bar{1}0]$ was cooled to ~58K and a number of field sweeps in and outside of the skyrmion phase were performed. In addition, DC magnetization measurements were performed in a PPMS system with ACMS II by our collaborators (group of Sunxiang Huang at the University of Miami). Figure 5.2 shows dM/dH and $\kappa_{xy} = \kappa_{yy} \frac{\nabla_y T}{\nabla_x T}$ as functions of magnetic field. Evidently, the skyrmion thermal Hall signal is below the level of detection, which is determined by the sensitivity of the thermocouple.

Even though measurement of the skyrmion thermal Hall yielded a null result, thermal conductivity in zero field showed a surprisingly high magnitude at low temperatures, which motivated further investigation.

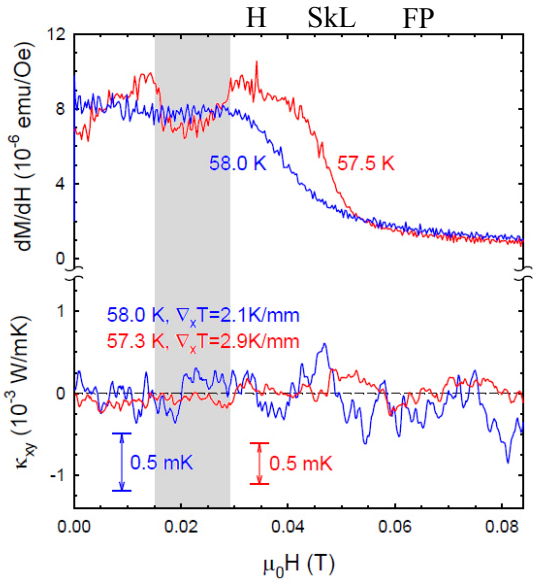

Figure 5.2. dM/dH and κ_{xy} as functions of magnetic field in the skyrmion phase (red) and above T_c (blue). Shading indicates the skyrmion phase (SkL).

5.2 Thermal conductivity with heat flow along [111]

5.2.1 Overview

This study presents the results of thermal conductivity measurements of Cu_2OSeO_3 samples with heat flow $\vec{J}_q || [111]$ and external magnetic field $\vec{H} || [1\bar{1}0]$. Single crystal samples were cut from different bulk single crystal specimens and the orientation and crystalline quality were verified by X-ray diffraction. The experimental setup used for thermal conductivity measurements is described in Section 3.4.3. Temperature-dependent thermal conductivity in $H = 0$ kOe and $H = 50$ kOe as well as magnetic-field-dependent thermal conductivity measurements were performed. Analysis of the data reveals that thermal conductivity can be separated into additive contributions from phonons and magnons. The extracted magnon thermal conductivity with the magnitude of ~70 W/mK at 6K greatly exceeds that measured in any other ferro- or ferrimagnet. Both phonons and

magnons conduct heat in the boundary-limited regime at low temperatures, while Poiseuille flow of magnons in the temperature region 2K < T < 10 K was identified.

5.2.2 Thermal Conductivity in Zero Magnetic Field

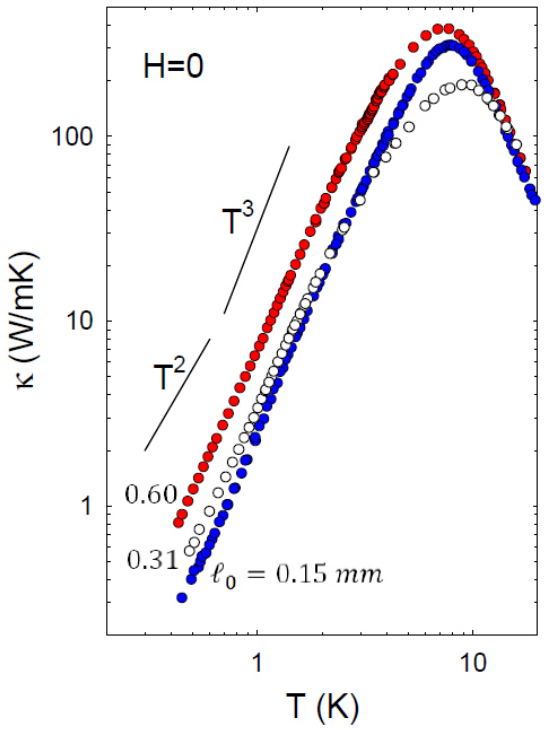

Figure 5.3. Temperature dependence of thermal conductivity for three samples with varying transverse dimensions l_0 in H = 0 kOe.

The zero-field thermal conductivity (κ) of three samples with differing transverse dimensions ($l_0 = 2\sqrt{a/\pi}$, where a is the cross-sectional area) are shown in Figure 5.3 for the temperature range 0.5 K < T < 20K and zero magnetic field is shown in Figure 5.3. At very low T, κ scales with the transverse dimension l_0, indicating that scattering from boundaries is the dominant relaxation mechanism with mean-free paths approaching the value of l_0 as $T \rightarrow 0$ K (ballistic regime, see Section 5.2.4). The thermal conductivities have maxima at ~8 K and reach ~400 W/mK for the largest sample. The magnitude of κ at

the peak is usually determined by defect scattering, therefore slight differences between the three samples can be attributed to different defect concentrations. Additionally, at low temperatures $\kappa(T)$ strongly deviates from the T^3 behavior expected for lattice thermal conductivity of an insulator. This is due a magnon contribution to κ (see Section 5.2.3).

5.2.3 Magnetic Field Dependence of Thermal Conductivity

Magnetic field dependence of thermal conductivity was measured at a series of fixed field values from -50 to 50 kOe while keeping the base temperature fixed. The results of the measurements from 0 to 50 kOe for samples with transverse dimensions $l_0 = 0.15$ mm and 0.31 mm are shown in Figure 5.4.

The first key feature of the data is the saturation of κ at low temperatures as magnetic field approaches 50 kOe in the field polarized (collinear) phase. In the presence of external magnetic field at low temperatures, the magnon dispersion relation can be approximated as $\hbar\omega_k = Dk^2 + g\mu_B H$. An increasing magnetic field suppresses magnon population (Eq. 2.1). In the case when magnetic field is strong enough $g\mu_B H \gg k_B T$, thermal conduction by magnons is completely suppressed and the total thermal conductivity is determined purely by the lattice contribution. At low temperatures the suppression occurs at $g\mu_B H/k_B T \approx 6$, which explains why the saturation is not observed in the T = 5.2 K data (lower panel of Figure 5.4a) – the estimated field strength required to suppress all magnons is approximately 220 kOe. The suppression at 50 kOe occurs for temperatures below 1.2 K.

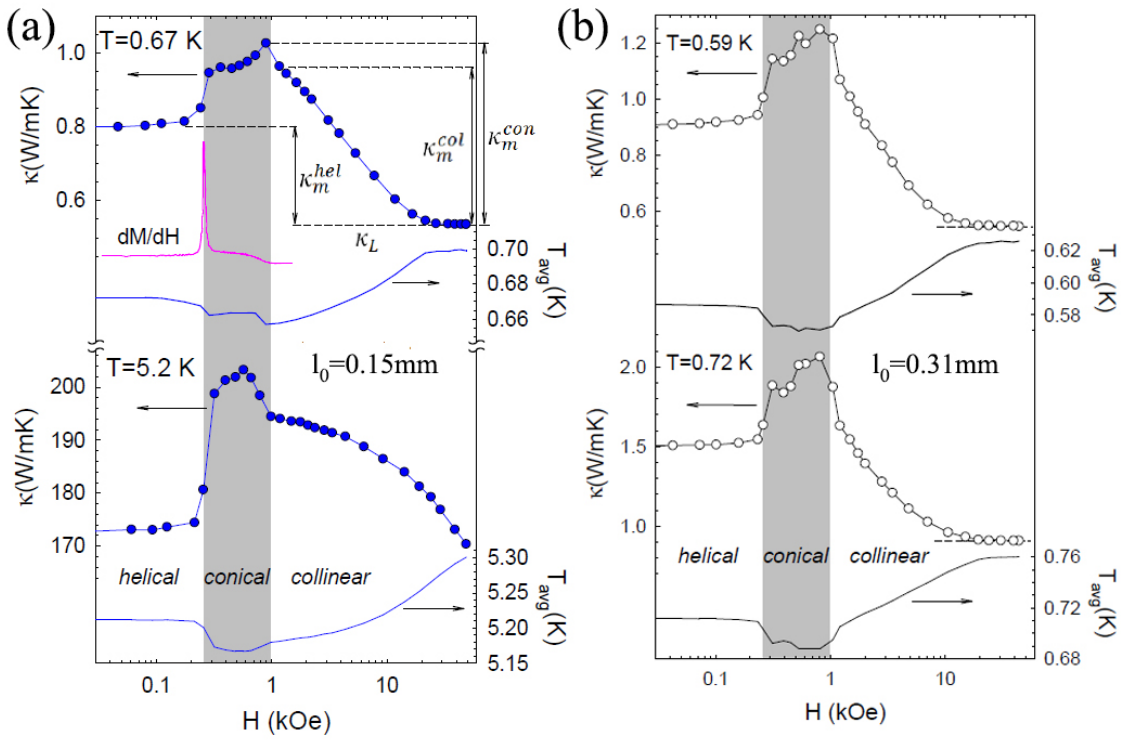

Figure 5.4. Magnetic field dependence of thermal conductivity, average temperature, and dM/dH for samples with transverse dimensions $l_0 = 0.15$mm (a) and 0.31mm (b).

We assume weak phonon-magnon interactions, that imply simple additive contributions to the total thermal conductivity from phonon (L) and magnon (m) systems $\kappa = \kappa_L + \kappa_m$. We take the saturation value to be equal to the lattice thermal conductivity κ_L and compute the magnon thermal conductivity in each spin phase ($\kappa_m^{hel}, \kappa_m^{con}, \kappa_m^{col}$ in Figure 5.4a) at low temperatures by direct subtraction.

The second feature is the sharp increase in thermal conductivity at the helical-conical transition. This jump is unlikely to be caused by changes in the magnetic texture, as specific heat does not exhibit similar behavior at the transition (see Figure 4.4), therefore, the effect is caused by the change in magnon scattering. It is reasonable to attribute the observed behavior to the transition from the multidomain state in the helical phase to the single domain conical phase. Evidently, domain boundaries in the helical phase

are very effective at scattering magnons and cause a considerable suppression of thermal conductivity. Interestingly, the increase of thermal conductivity in the conical phase opposes the decrease in specific heat.

5.2.4 Magnon Thermal Conductivity

In order to perform the separation of magnon contribution from the total thermal conductivity, lattice thermal conductivity at temperatures where the saturation does not occur at the magnetic field of 50 kOe was computed using the Calloway model (Section 2.1.3). The parameters of the model were constrained to satisfy the following conditions:

1) κ_L fits the low temperature ($T < 1.2$K) 50 kOe data, where the direct suppression is observed;
2) κ_L fits the high temperature ($T < 1.2$K) zero-field data, where κ shows negligible field dependence;
3) the maximum in $\kappa_m^{con} = \kappa - \kappa_L$ occurs at the same temperature where $\kappa_m^{con} - \kappa_m^{hel}$ peaks;
4) $\kappa_L < \kappa$.

Normal and resistive scattering rates were taken to have the form

$$\tau_N^{-1} = \gamma A x^2 \mathrm{T}^4 \,. \tag{5.1a}$$

$$\tau_U^{-1} = \frac{v}{l_0} + A x^2 \mathrm{T}^4 \exp\left(\frac{\theta_D}{bT}\right) + \mathrm{C}x^4 T^4, \tag{5.1b}$$

where $A, b, C, and\ \gamma$ are free parameters. Figure 5.5 shows the obtained fits to the lattice thermal conductivity, while the parameter ranges are summarized in Table 5.1.

Table 5.1. Ranges of parameters from Callaway modeling of κ_L.

l_0 (mm)	v (km/s)	A (10^4 K^{-4})	b	C (K^{-4})
0.15	2.06 − 2.15	1.8 − 2.0	6.6 − 6.9	10 − 15
0.31	2.15 − 2.35	1.5 − 1.8	6.0 − 6.6	80 − 110
0.60	2.06 − 2.3	1.75 − 2.0	6.3 − 6.6	34 − 40

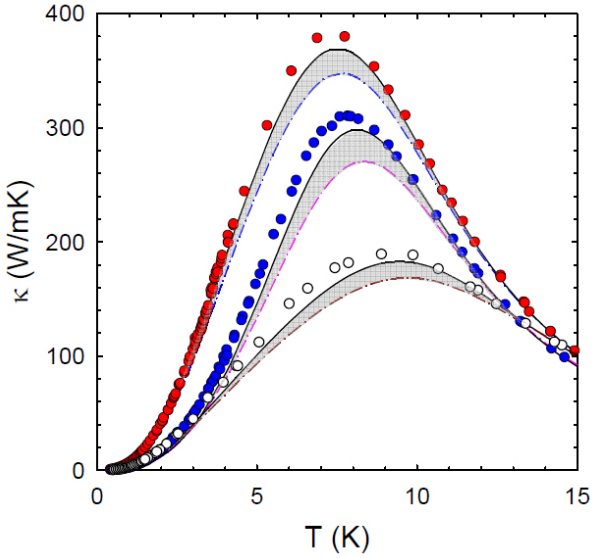

Figure 5.5. Zero field thermal conductivity from Figure 5.3 (circles) and κ_L computed for the two ends of the parameter range (solid and dash-dotted curves). Shaded regions correspond to parameter ranges from Table 5.1.

Magnon thermal conductivity in the conical phase was calculated by subtracting κ_L, computed using the mean values of the ranges from Table 5.1, from the maximum total thermal conductivity in the conical phase. Obtained κ_m^{con} reaches a value of ~70 W/mK at the peak near 5K, which is the record high magnitude for magnon thermal conductivity of ferro- and ferrimagnetic materials. Moreover, for T > 1K κ_m^{con} of the two least defective samples (blue and green circles in Figure 5.6) grows with temperature at a rate much faster than T^2 predicted by linear spin wave theory (Eq. 2.23). This temperature behavior can be explained by two possible mechanisms: 1) magnon-phonon drag, 2) Poiseuille flow of

magnons. The former predicts a much stronger temperature dependence ($\propto T^4$) [63], so we explore the second possibility in Section 5.2.5.

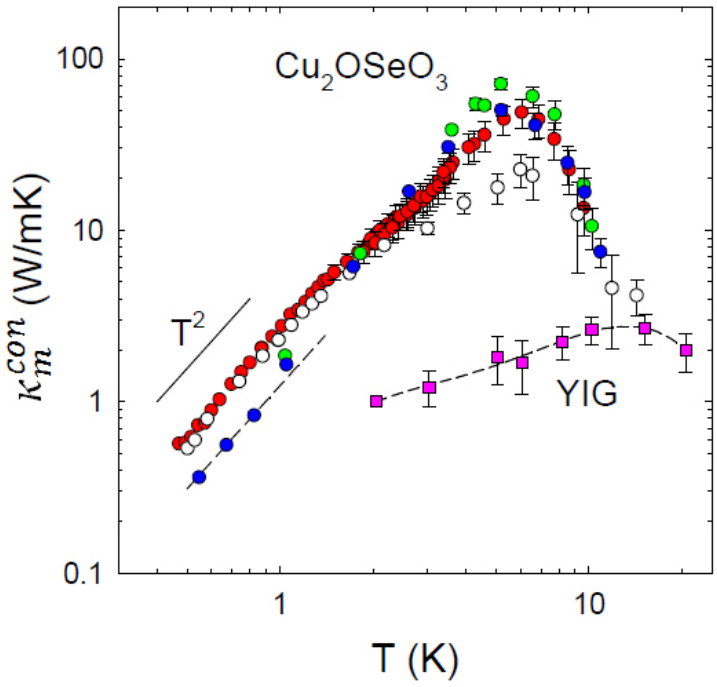

Figure 5.6. Magnon thermal conductivity in the conical phase (circles). Magnon thermal conductivity of YIG (squares) from Ref. [64].

5.2.5 Ballistic Regime of Phonon and Magnon Conduction

Figure 5.7 shows the low-temperature thermal conductivity at H = 0 kOe and H = 50 kOe. At 50 kOe κ is proportional to T^3, further corroborating the argument that high-field thermal conductivity is purely due to the lattice at low temperatures (Section 5.2.3). The expression for low temperature, boundary-limited thermal conductivity (Eq. 2.15b) was used to model the H = 50 kOe data, yielding phonon mean-free paths $l_{ph} \simeq$ 0.16, 0.24, 0.59 mm, consistent with the effective transverse dimensions of the samples.

The model for boundary limited magnon thermal conductivity (Eq. 2.23b) was used to fit the low-temperature part of Figure 5.6 data, yielding magnon mean-free paths

$l_m \simeq 0.14, 0.25, 0.28$ mm, which agree well with the transverse dimensions except in the case of the largest sample, where a single magnetic domain might not be as big as the crystal.

The above results confirm that both magnons and phonons conduct heat in the boundary-limited (ballistic) regime at low temperatures.

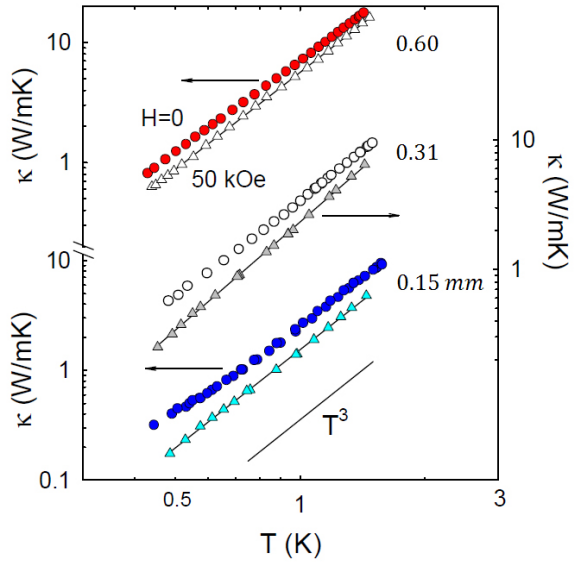

Figure 5.7. Low temperature thermal conductivity of the three samples from Figure 5.3: $\kappa(H = 0$ kOe) – circles, $\kappa(H = 50$ kOe) – triangles. Solid lines – fits to Eq. 2.15b.

5.2.6 Poiseuille Flow of Magnons

Microscopically Poiseuille flow is characterized by quasiparticle mean-free paths greatly exceeding the limits imposed by boundary scattering [65], [66]. Many momentum conserving scattering events occur before the particle thermalizes at the boundary, effectively resulting in a random walk with step size l_N. This effect is only possible in a narrow range when $l_N < l_0/2 < (l_N l_U)^{1/2}$ and the mean-free path approaches $\frac{{l_0}^2}{4l_N} \gg l_0$. The model for Poiseuille flow was developed by Alvarez and Jou [67]

$$\kappa_m = \frac{1}{3} C_m v_m \left[l_U^B (1 - \Sigma) + l_U F(L_{eff}) \Sigma \right], \tag{5.2a}$$

$$F(L_{eff}) = \frac{1}{2\pi^2} \left(\frac{L_{eff}}{l} \right)^2 \left[\sqrt{1 + 4\pi^2 \left(\frac{l}{L_{eff}} \right)^2} - 1 \right], \tag{5.2b}$$

where $\Sigma = 1/(1 + l_N/l_U)^2$, $L_{eff} = \pi l_0/2\sqrt{2}$, $l = \sqrt{l_N l_U}$, $l_U = (1/l_{3U} + 1/l_{4U} + 1/l_i)^{-1}$, $l_U^B = (1/l_0 + 1/l_U)^{-1}$, and l_{3U}, l_{4U}, $1/l_i$ are the mean-free paths corresponding to 3-magnon, 4-magnon, and impurity scattering processes. The mean-free paths were calculated using the thermally averaged scattering rates from Section 2.2.2 and are presented in Figure 5.8a. Magnon thermal conductivities calculated for the three samples with different transverse dimensions l_0 using Eq. 5.2a are in good agreement with the data, providing support that magnon heat conduction is in Poiseuille regime.

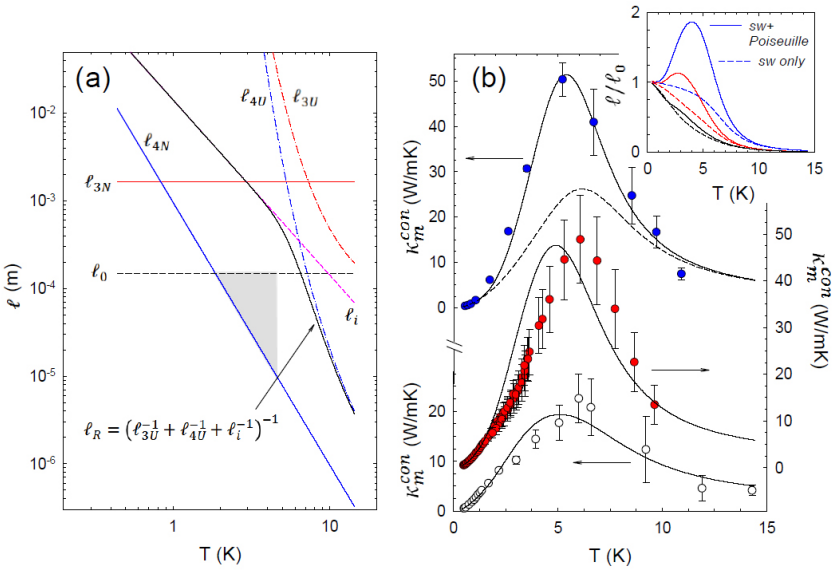

Figure 5.8. (a) Magnon mean-free paths for 3-magnon and 4-magnon normal (3N, 4N), umklapp (3U, 4U) processes, elastic impurity scattering (i), and total resistive scattering (R). The Poiseuille conditions are met in the shaded region. (b) κ_m^{con}(T) for the three samples from Fig. 5.3. The solid curves are model predictions (Eq. 5.2a). The dashed curve for the l_0 = 0.15 mm specimen represents the spin-wave contribution alone without Poiseuille enhancement. Inset: magnon mean-free paths from the model, normalized by low-T boundary-limited values, for each sample.

5.2.7 Outlook

Due to its record high magnon thermal conductivity, Cu_2OSeO_3 is a model system for probing long-wavelength magnon dynamics in helical magnets. Studies of magnon heat conduction and magnon-phonon interactions are of great importance in the fields of spin caloritonics [68] and magnon spintronics [69]. Also, thermal magnon currents are important in the field of skyrmion caloritonics because of spin-transfer torques thermal magnons induce on skyrmions [70], providing a means of manipulating skyrmions and domain walls [62], [71], [72] and giving rise to exotic effects such as topological magnon Hall and skyrmion Hall effects [73]. The recent identification of a previously unknown low-T skyrmion phase in Cu_2OSeO_3 [74] suggests the possibility of observing a magnon thermal Hall effect in this material [75], [76]. Yet another interesting effect has been proposed by Ulloa *et. al* for magnon dynamics in the Poiseuille regime [77]. Their calculations suggest that a sign change in the non-local spin Seebeck signal in the magnon fluid regime can be observed experimentally.

5.3 Thermal conductivity with magnetic field along [100] and [110]

5.3.1 Overview

In this section we present field-dependent thermal conductivity and magnetization data for several measurement configurations distinguished by the direction of the heat flow and magnetic field. When the field is in the [100] crystallographic direction, magnon thermal conductivity displays sharp features attributed to the transitions into tilted conical and low-temperature skyrmion phases. These features are explained by the effects of domain structure and anisotropic scattering on magnon heat transport. Overall, magnon

thermal conductivity measurements offer a great tool for probing spin-phase transitions and offer new insight into magnon transport in novel magnetic phases.

5.3.2 Thermal conductivity with magnetic field along [110]

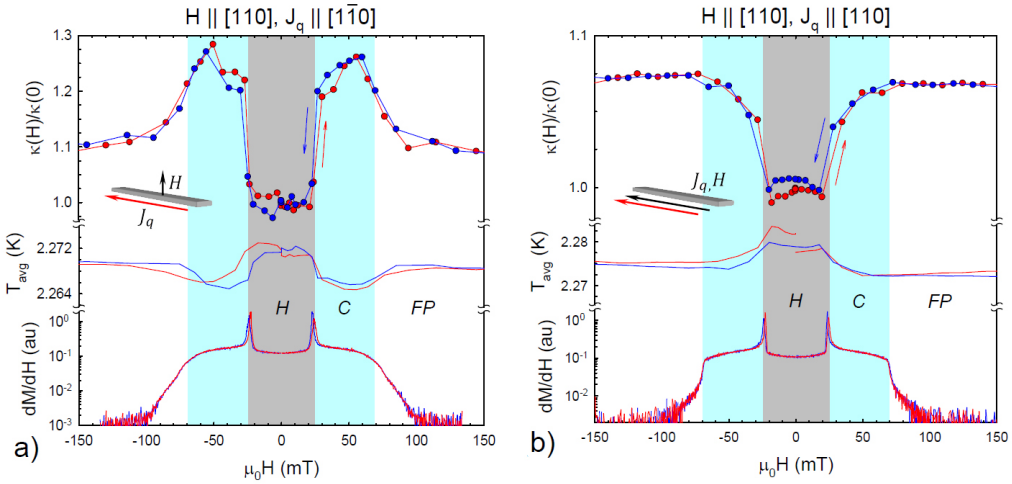

Figure 5.9. κ, T_{avg}, and dM/dH vs. field at T~2.3 K for heat flow perpendicular (a) and parallel (b) to magnetic field in [110] direction. Helical (H), conical (C), and field polarized (FP) spin phases are distinguished by shading. Red (blue) symbols depict increasing (decreasing) field magnitude.

Figure 5.9 presents field-dependent thermal conductivity, average temperature, and dM/dH data for two specimens with magnetic field along the [110] crystallographic direction and heat flow perpendicular (a) and parallel (b) to the field. As discussed in Section 5.2.3, changes in thermal conductivity with respect to magnetic field above the field-suppressed (lattice) value can be attributed to changes of the magnon contribution and the sharp increase at the helical-to-conical transition for both orientations corresponds to the disappearance of magnetic domain boundary scattering at the transition from a multidomain to a single domain phase. A smaller upturn in κ for the parallel orientation of field and heat current (Fig. 5.9b) suggests the presence of anisotropic magnon-phonon scattering possibly explained by anisotropic magnetoelastic effects or spin-orbit

interactions. Similarly to the [111] case, the behavior of gradual increase of thermal conductivity with the field in the conical phase past the H-C transition and suppression in high field are also observed for these orientations. Notable is the absence of hysteresis.

5.3.2 Thermal conductivity with magnetic field along [100]

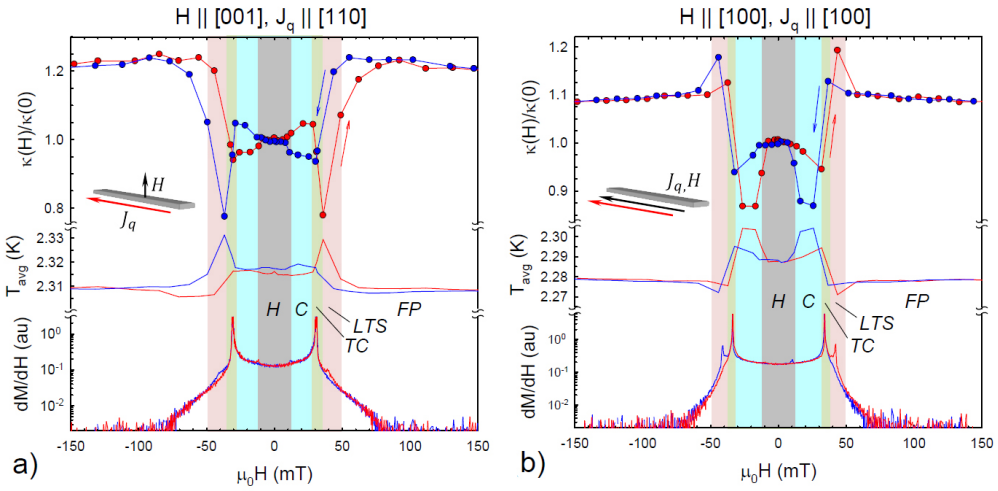

Figure 5.10. $\kappa(H)/\kappa(0)$, T_{avg}, and dM/dH vs. field at T~2.3 K for heat flow perpendicular (a) and parallel (b) to magnetic field in [100] direction. Helical (H), conical (C), and field polarized (FP) spin phases are distinguished by shading.

The [100] crystallographic direction is favored by cubic anisotropy terms for the orientation of the helical spiral upon cooling in zero field. The competition between anisotropy term and Zeeman terms in applied field is responsible for formations of two new spin phases – tilted conical (TC) and low-temperature skyrmion (LTS) – at low temperatures (see Section 4.2). When the magnetic field is along [100], thermal conductivity displays additional features at fields that coincide with transitions in and out of TC and LTS phases. Figure 5.10 shows $\kappa(H)/\kappa(0)$, T_{avg}, and dM/dH for this orientation of the field and heat flow perpendicular (along [110]) and parallel ([100]) to the direction of the field. The absence of a sharp increase in thermal conductivity at the H-C transition in these orientations can be explained by the conversion of three helical

domains into a single helical domain caused by a small external field in the H phase aligned with the preferred direction of helical modulation. Since there are no domain rotations, the domain wall scattering does not change through the transition.

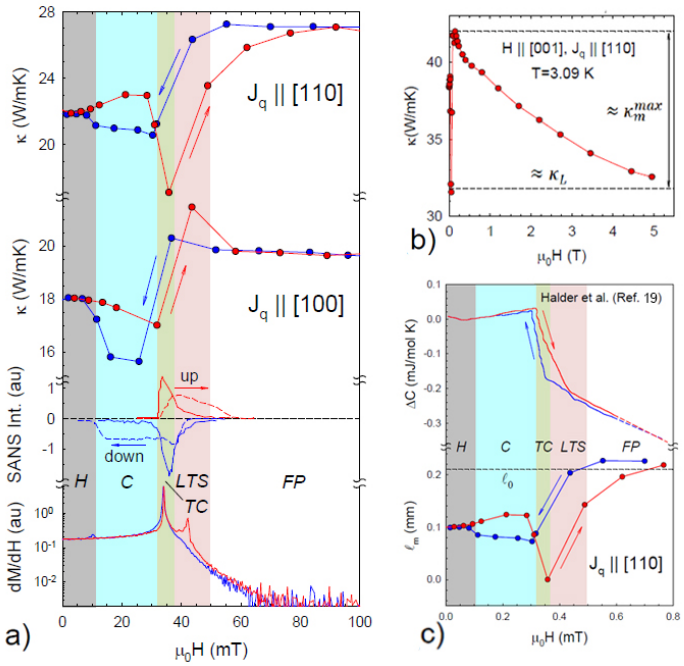

Figure 5.11. (a) Upper panels: the H > 0 portion of κ vs H from Fig. 5.10. Middle panel: SANS intensities for increasing ("up") and decreasing ("down") fields (from Ref. [55]) for the TC (solid curves) and LTS (dashed curves) phases. Field values for the SANS data were calibrated against peaks in dM/dH. Lower panel: dM/dH from Fig. 5.10b.

Strongly hysteretic features in conical, tilted conical, and low-temperature skyrmion phases are evident. Figure 5.11 displays thermal conductivity for $H > 0$ plotted against SANS intensities and dM/dH. SANS intensities form Ref. [55] for tilted conical and low-temperature skyrmion phases determine phase boundaries in the ascending and descending fields and the regions where phases coexist. First, we describe the features that distinguish the two orientations of the heat flow. In ascending field thermal conductivities in the conical phase exhibit opposite behaviors: κ for heat flow along [110] increases, while it decreases for heat flow along [100]. Opposite trends are also observed in ascending

field upon the transition into the tilted conical phase: J_q || [110] show a sharp drop, but for J_q || [100] κ rapidly grows. Then there are some common features for the two directions of J_q. Thermal conductivity keeps growing with ascending field in LTS phase and reaches its maximum value before the transition to the FP phase. In descending field κ in the region of TC and LTS phase coexistence is significantly smaller than in the ascending field. The latter features suggest that the domain structure in the region of coexistence of LTS and TC is responsible for significantly higher magnon scattering probabilities compared to the LTS phase and the region of LTS and TC coexistence.

Highly hysteretic behavior of the data in the regions of non-zero LTS intensities is explained by the strongly first-order character of transitions from all other phases to LTS. Topological robustness of the skyrmion lattice is caused by a large energy barrier required for creation of pairs of Bloch points (magnetic monopoles) [56],[57].

Field dependence of thermal conductivity extended to higher fields (Figure 5.11b) reveals that the magnitude of thermal conductivity at the sharp drop caused by the C to TC transition is very close to the field-suppressed (lattice) value. Effectively, upon entering the TC phase magnon heat conduction practically drops to zero. We propose that this is caused by the domain structure in the TC phase that results in highly anisotropic scattering of magnons with momenta transverse to the applied field.

The comparison of field-dependent heat capacity data from Ref. [55] with the thermal conductivity data supports our interpretation of changes of magnon scattering character across the phase boundaries (Figure 5.11c). Magnon mean path, computed using the kinetic theory expression $l_m = 3\kappa_m / C_m v_m$, provides additional insight into characteristic length scales involved in magnon conduction in domain structures of various

spin phases. Notably, the mean free paths in the field polarized phase are equal to the transverse dimension of the sample l_0.

5.3.3 Outlook

Critical suppression of magnon current at the conical to tilted conical phase boundary might be utilized in the design of a spin current switch, as the observed behavior suggests that the spin currents associated with thermal flow of magnons can be reduced to zero in a very narrow magnetic field range.

Detailed microscopic pictures of domain structures in new exotic chiral spin phases are not well established but might be of great importance for the development of magnonic and skyrmionics memory devices. Magnon currents and associated spin currents provide a mechanism for domain wall manipulation through spin transfer torques, thus fundamental understanding of relevant length scales of magnon transport is crucial in device design.

Chapter 6. Longitudinal Spin Seebeck Effect in Cu_2OSeO_3

6.1 Overview

Recent theoretical efforts come to a consensus that spin Seebeck effect has its origins in thermal magnon currents [26], [83], suggesting that spin Seebeck is observable in magnetic materials with large magnon thermal conductivities. Rich spin phase diagram accompanied by substantial magnon thermal conductivity in each phase establishes Cu_2OSeO_3 as an excellent candidate for studies of thermal spin transport in chiral phases – a research avenue that has not received a lot of attention, possibly because the majority of chiral magnets are metallic, making it difficult to separate pure spin current effects from spin polarized charge current contributions.

Table 6.1. Sample geometry.

#	l (mm)	$\vec{J}_q$ ($\hat{l}$) direction	w (mm)	$\vec{H}$ ($\hat{w}$) direction	t (mm)
1	5.00	$[111]$	1.11	$[1\bar{1}0]$	0.26
2	5.00	$[111]$	0.86	$[1\bar{1}0]$	0.20
3	3.68	$[111]$	0.75	$[1\bar{1}0]$	0.11
4	0.75	$[110]$	3.75	$[1\bar{1}0]$	1.43

This chapter presents the results of our studies of longitudinal spin Seebeck effect (LSSE) in Cu_2OSeO_3 when heat flow is parallel to the $[111]$ crystallographic direction and magnetic field is along $[1\bar{1}0]$. The experimental setup used for the measurements is described in Section 3.4.4. Table 6.1 provides details about the geometries of the samples measured.

We begin the discussion by addressing the concerns of contamination of measured signals by various spurious effects. Next the magnetic field dependence of the spin Seebeck

coefficient S_{LSSE} in the context of various spin phases is discussed. Analysis of temperature dependence of S_{LSSE} presented next provides insight into relevant length scales. We conclude by mentioning some interesting effects of surface preparation on observed spin Seebeck signal and discuss the peculiar effect Joule heating in the platinum film has on thermal conductivity.

6.2 Platinum Film Characterization

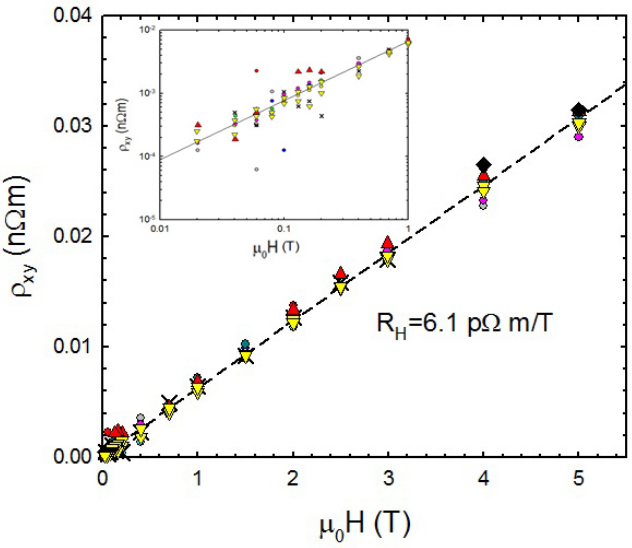

Figure 6.1. Field dependence of Hall resistivity of a Pt film on Cu_2OSeO_3 at 6 temperatures in the range 0.4-10 K. The inset shows the linearity of the data near 0T.

Huang *et al.* [85] observed effects of proximity magnetization in transport properties of platinum films deposited on ferromagnetic insulators caused by the proximity to Stoner instability of Pt. Here we present our results of Pt film characterization in an attempt to address the concerns of spurious anomalous Nernst effect contaminating LSSE signal. For a discussion of platinum film preparation procedures refer to Section 3.3.

The resistivity of our 8-10 nm Pt films on Cu_2OSeO_3 of around 3 μΩcm is in good agreement with literature values for thin films [85]. Figure 6.1 shows magnetic field

dependence of Hall resistivity ρ_{xy} for a Pt film on Cu_2OSeO_3 (crystal #4) at 6 temperatures in the range 0.4-10 K. Hall resistivities are linear down to zero field and the fits to data pass through the origin – signs that the anomalous Hall effect associated with proximity magnetization effect is not present in Pt/Cu_2OSeO_3 heterostructures.

Additionally, we analyze the effects of weak localization in the temperature dependence of Pt film resistivity. Figure 6.2a presents temperature dependence of $\frac{\Delta R}{R} = \frac{R-R_{min}}{R}$. The logarithmic rise is caused by weak localization effects and obeys

$$\frac{\Delta R}{R} = -\frac{e^2}{2\pi^2\hbar} R_{\square}(T_0)\alpha_T ln\left(\frac{T}{T_0}\right), \tag{6.1}$$

where $R_{\square}$ is the sheet resistance, T_0 is the temperature of resistance minimum, and α_T is the strength of the weak localization effect [86]. The value of $\alpha_T = 0.998$ (Figure 6.2b) is in good agreement with the literature value of α_T =1.01±0.07.

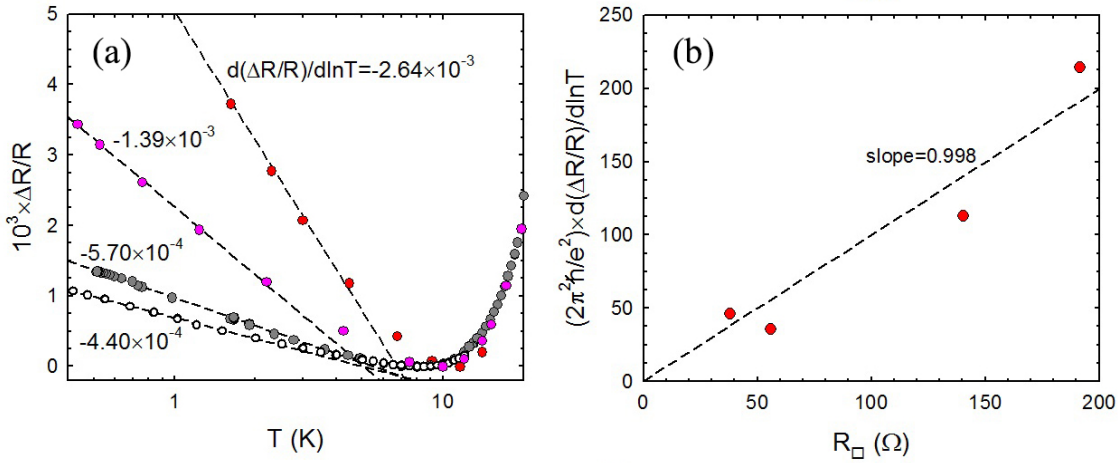

Figure 6.2. (a) Low-T logarithmic-in-T resistance increase for four Pt films. (b) Scaling of ln (T) resistance rise with sheet resistance.

6.3 Magnetic Field Dependence of Spin Seebeck Coefficient

As was discussed in Section 3.4.4, the voltage difference between the two ends of the platinum film V_{pt} is directly measured by a nanovoltmeter. Acquisition of field-

dependent $V_{pt}(H)$ is performed using the following procedure: 1) base temperature and heater power are stabilized at a desired value and kept constant throughout the measurement, 2) V_{pt} is measured at a number of fixed field values from H = 0 kOe up to 50 kOe, then down to -50 kOe using the same field setpoints, and back up to zero. Eventually, we discovered that the complete field loop does not produce any significant hysteresis in the voltage signal, so we measured V_{pt} at a series of fixed field values between 50 kOe and -50 kOe (subsequently referred to as "field sweeps") in either ascending or descending field. For the remainder of the discussion we will focus on experimental data obtained for sample #2, that showed the biggest overall spin Seebeck effect. The results for other samples agree with the discussion presented below qualitatively.

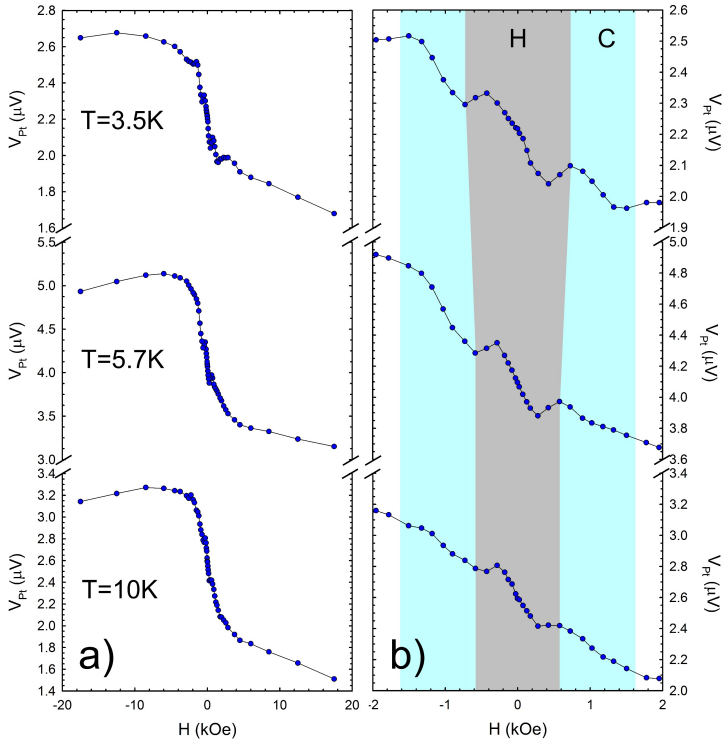

Figure 6.3. (a) Antisymmetric field dependence of V_{pt} for three temperatures. (b) Expanded field scale showing boundaries of helical (H) and conical (C) spin phases.

Figure 6.3a shows V_{pt} vs H data for three selected temperatures. Apparent are the odd symmetry of the signal and a thermal offset at $H = 0$. The expanded field scale in Figure 6.3b reveals sharp asymmetric features of the signal that line up with identified spin phase boundaries.

Further analysis of the data involves the step that eliminates the thermal offset voltage, sample geometry dependence, and temperature gradient dependence.

We calculate the LSSE coefficient S_{LSSE} (Eq. 2.41), a quantity that purely depends on properties of the materials constituting the heterostructure and characteristic parameters describing the interactions at their interface using the equation

$$S_{LSSE} = \frac{V_{Pt}(H) - V_{Pt}(-H)}{2w} \frac{l_{\Delta T}}{\Delta T}. \tag{6.1}$$

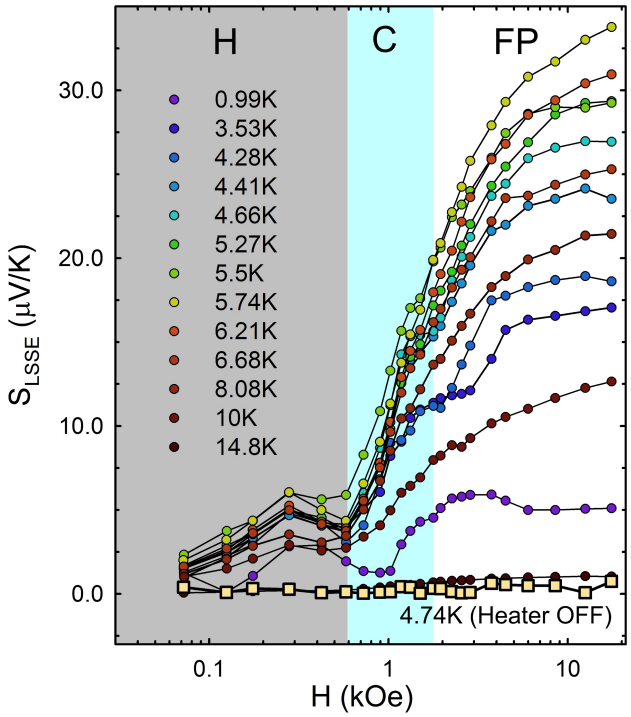

Figure 6.4. Field dependence of S_{LSSE} at temperatures between 1 K and 15 K (circles). Signal is absent when the heater is off (squares).

Figure 6.4 shows the spin Seebeck coefficient as a function of magnetic field for several temperatures between 1 K and 15K with the maximum value reaching ~30 μV/K in the collinear phase. Also shown in the figure is the spin Seebeck coefficient when the heater output is zero (squares in Figure 6.4); in this case S_{LSSE} is negligibly small as expected.

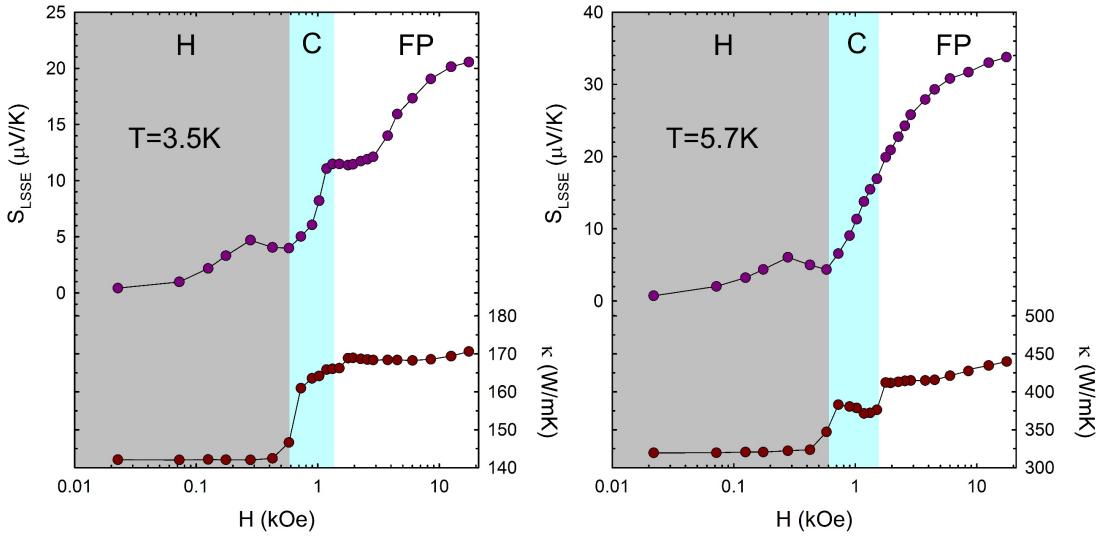

Figure 6.5. Field dependence of S_{LSSE} (upper panel) correlated against thermal conductivity (lower panel) for T = 3.5K and 5.7K.

A more fundamental understanding of behavior of spin Seebeck coefficient in field is offered by its comparison with thermal conductivity, simultaneously measured with S_{LSSE}. The *in situ* thermal conductivity measurement is one of the advantages the measurement technique in this work offers over conventional LSSE setups (see Section 3.4.4). Figure 6.5 correlates spin Seebeck coefficient against thermal conductivity for T = 3.5 and 5.7 K. Despite no observation of suppression of κ in high field (magnetic fields on the order of 200 kOe are required to completely depopulate spin waves at presented temperatures), the argument (developed in Section 5.2.3), that changes of thermal conductivity in field can be attributed to changes in the magnon contribution, still applies

here. This presents us with a great opportunity to analyze correlations between heat and spin currents associated with a thermally driven flow of magnons. Magnon thermal conductivity in the helical phase is finite (~15% of total κ) and does not change in field. Spin Seebeck effect in the helical phase starts out at zero and gradually increases before making a slight downturn upon approaching the H-C transition.

This difference in behavior can be explained by the absence of net magnetization parallel to the field, required for spin pumping, in the multidomain helical phase, whereas the same magnons are still capable of producing a net flux opposite to the temperature gradient. Gradual rotations of helical domains in increasing small field could result in a net spin current, explaining the rise of S_{LSSE}, but seem to have no effect on heat conduction. In the conical phase, as the conical angle decreases in increasing field, a bigger component of precessing magnetization becomes parallel to the field, resulting in more efficient spin pumping. Interestingly, only field sweeps at temperatures below approximately 4 K show prominent features related to the C-FP phase transition. Perhaps, this could be explained by higher thermal fluctuations of spins smearing a clear boundary between low-angle conical and collinear phases (when it comes to the effective component of spin polarization parallel to the field). These thermal fluctuations are then suppressed by the increasing field in the FP phase eventually resulting in saturation of S_{LSSE} at its maximum value, as spins precessing around the direction of the field provide maximum pumping efficiency. Field dependence of spin Seebeck effect in high field closely resembles the behavior of thermal conductivity, and suppression due to magnon depopulation is not observed at these temperatures, though the 0.99 K data in Figure 6.4 appears to show this trend. Generally, acquisition of spin Seebeck data at low temperatures is very challenging, since achievable

temperature differences are strongly limited by the geometric factor of the sample and spin Seebeck voltage becomes rather small and noisy when the gradient is small.

6.4 Temperature Dependence of Spin Seebeck Coefficient

6.4.1 Results

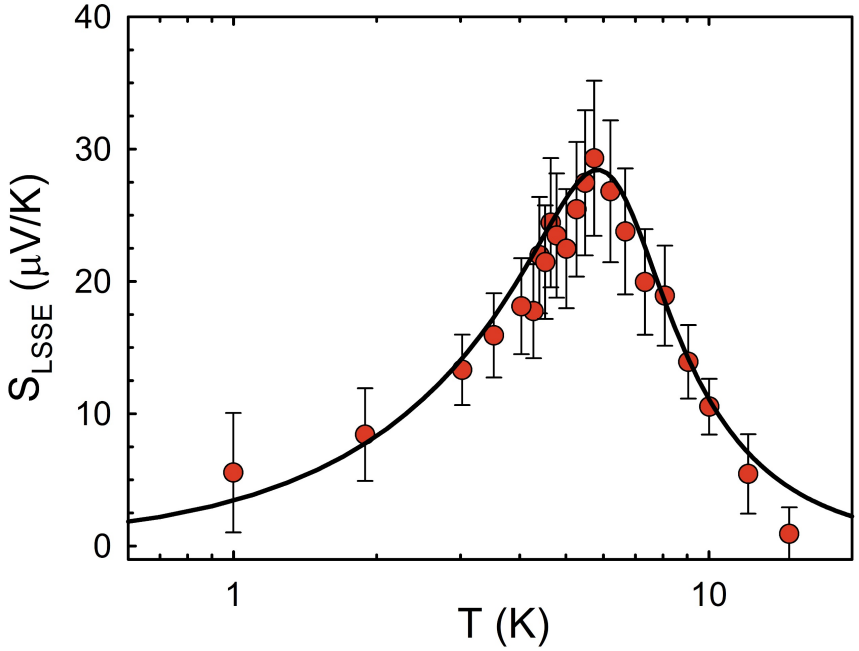

Figure 6.6. Temperature dependence of S_{LSSE} at H = 4.5 kOe in the FP phase (circles). The peak value of ~30 μV/K occurs at $T \approx 6$ K. Data is fit with model from Ref. [27].

Figure 6.6 depicts the temperature dependence of spin Seebeck coefficient in the field polarized phase. S_{LSSE} peaks at a value of ~30 μV/K at $T \approx 6$ K, which is approximately three times bigger than the value of ~9 μV/K of YIG at its peak ($T \approx 31$ K) [87]. Bulk magnon theory from Ref. [27] described in more detail in Section 2.3 was used to fit the experimental data. Error bars incorporate the uncertainties in the measurement of the temperature gradient, noise levels of the Pt voltage, and temperature instabilities during field sweeps.

6.4.2 Modeling

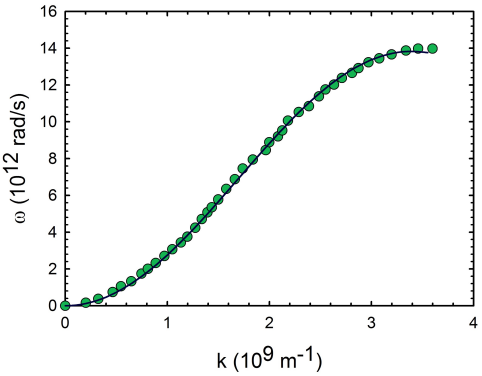

Figure 6.7. Lowest branch of magnon dispersion.

Magnon dispersion from Ref. [91], fit with $\omega_k = \omega_{ZB}(1 - \cos \pi k/2k_m)$ giving $\omega_{ZB} = 6.9 \times 10^{12}\, rad/s$, $k_m = 1.7 \times 10^9\, m^{-1}$, was used in the calculation (Figure 6.7). Thermally averaged magnon-magnon scattering rates were calculated using Eq. 2.26 and parameters $T_e = 4.2\, K$, $T_d = 0.004$K, $S = 1$, $c = 10$ ppm, and the numeric prefactor for τ_{4U}^{-1} was increased by 15. Magnon-phonon lifetime was taken to be $\tau_{mp} = 2.5 \times 10^{-7} T^{-3/2}\, s$. Other parameters include thickness of platinum film $t_N = 10$ nm, platinum film resistance $R_N = 120\, \Omega$, spin diffusion length in platinum (value for YIG from Ref. [88]) $\lambda_N = 3.7$ nm, platinum spin-Hall angle $\theta_{SH} = 0.05$, gyromagnetic ratio $\gamma = 1.82 \times 10^{11}\, m/As$ [89], saturation magnetization $4\pi M_s = 1.15 \times 10^5\, A/m$, effective spin mixing conductance $g_{eff} = 9 \times 10^{17}\, m^{-2}$, and magnon lifetime of k = 0 magnons $\tau_0 = 6.6 \times 10^{-11} s$.

6.4.3 Comparison with Magnon Thermal Conductivity

Figure 6.8 shows temperature dependencies of spin Seebeck coefficient in the FP phase and magnon thermal conductivity of the $l_0 = 0.6\, mm$ sample from Figure 5.6, separated from the lattice following the procedure outlined in Section 5.2.4. The two

closely correlate, suggesting that thermal magnons and magnons responsible for the pumping of spin current into the platinum film are of similar energy scale, thus providing evidence for thermal magnon origin of spin Seebeck effect in Cu_2OSeO_3.

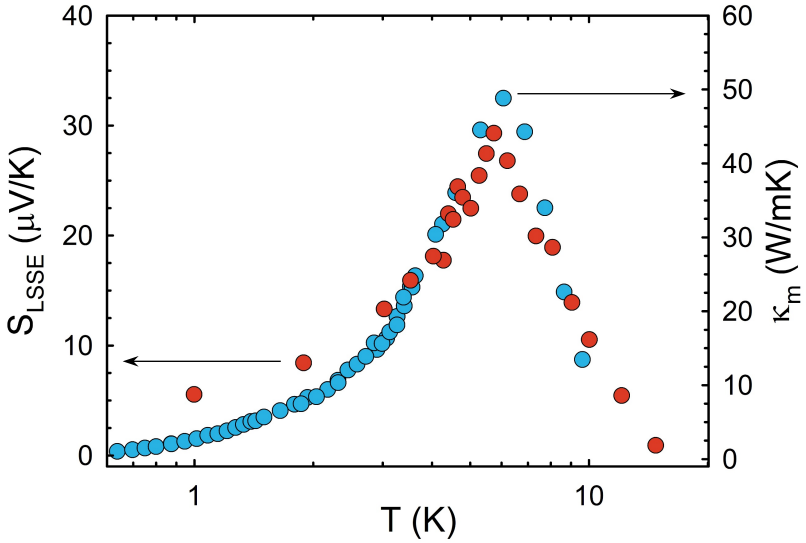

Figure 6.8. Field dependence of S_{LSSE} (orange circles) correlated against magnon thermal conductivity of sample #1 (blue circles).

6.4.4 Magnon Diffusion Length

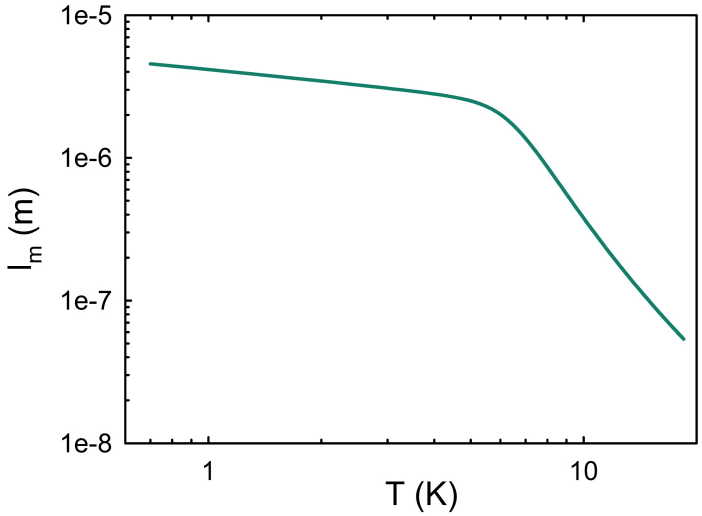

Figure 6.9. Magnon diffusion length vs temperature.

We have calculated the temperature dependence of magnon diffusion length l_m (Eq. 2.36) using thermally averaged magnon lifetimes. The results displayed in Figure 6.9 show that at 2 K $l_m \approx 3.5\ \mu m$, compared to $\sim 10\ \mu m$ for YIG [90]. Though unlikely to be probed by thickness dependent measurements similar to Ref. [93], measurements of non-local spin Seebeck effect might provide additional information about relevant length scales.

6.5 Outlook

In this chapter we presented experimental evidence establishing the presence of spin Seebeck effect in Cu_2OSeO_3. The unique measurement setup we employed allowed us to gain a lot of insight into the correlations between thermal magnon transport and thermal spin currents responsible for LSSE. More detailed analysis of temperature dependence based on spectral dependencies of magnon-magnon and magnon phonon interactions [94],[95] could contribute to the current discussion of the role of subthermal magnons in spin Seebeck effect [96]-[98]. Although the scope of this work was limited to only one relative orientation of heat flow and magnetic field, our thermal conductivity measurements suggest that further studies of LSSE in other directions will be informative. In addition, exploration of spin Seebeck effect in Cu_2OSeO_3 in the two skyrmion phases can provide great insight into skyrmion spin transport and its interactions with thermally generated spin excitations and phonons.

REFERENCES

[1] K. Uchida, T. Ota, H. Adachi, J. Xiao, T. Nonaka, Y. Kajiwara, G. E. W. Bauer, S. Maekawa, and E. Saitoh, "Thermal Spin Pumping and Magnon-Phonon-Mediated Spin-Seebeck Effect," J. Appl. Phys., 111, 103903, 2012.

[2] T. J. Seebeck, "Über den Magnetismus der Galvanischen Kette," Abh. preuss. Akad. Wiss, Akademie der Wissenschaftten aus den Jahren 1820-1821, 289–346, 1821.

[3] K. Uchida, S. Takahashi, K. Harii, J. Ieda, W. Koshibae, K. Ando, S. Maekawa, and E. Saitoh, "Observation of the Spin Seebeck Effect," Nature, 455, 778-781, 2008.

[4] K. Uchida, M. Ishida, T. Kikkawa, A. Kirihara, T. Murakami, and E. Saitoh, "Longitudinal Spin Seebeck Effect: from Fundamentals to Applications," J. Phys.: Condens. Matter, 26, 389601, 2014.

[5] C. M. Jaworski, J. Yang, S. Mack, D. D. Awschalom, J. P. Heremans, and R. C. Myers, "Observation of the Spin-Seebeck Effect in a Ferromagnetic Semiconductor," Nat. Mater., 9, 898, 2010.

[6] K. Uchida, J. Xiao, H. Adachi, J. Ohe, S. Takahashi, J. Ieda, T. Ota, Y. Kajiwara, H. Umezawa, H. Kawai, G. E. W. Bauer, S. Maekawa, and E. Saitoh, "Spin Seebeck Insulator," Nat. Mater., 9, 894, 2010.

[7] J. Xiao, G. E. W. Bauer, K. Uchida, E. Saitoh, and S. Maekawa, "Theory of Magnon Driven Spin Seebeck Effect," Phys. Rev. B, 81, 214418, 2010.

[8] M. Agrawal, V. I. Vasyuchka, A. A. Serga, A. D. Karenowska, G. A. Melkov, and B. Hillebrands, "Direct Measurement of Magnon Temperature: New Insight into Magnon- Phonon Coupling in Magnetic Insulators," Phys. Rev. Lett., 111, 107204, 2013.

[9] R. Peierls, "Zur kinetischen Theorie der Warmeleitung in Kristallen," Ann. Phys., 395, 1055–1101, 1929.

[10] A. A. Maznev, O. B. Wright, "Demystifying Umklapp vs Normal Scattering in Lattice Thermal Conductivity," Am. J. Phys., 82, 1062, 2014.

[11] A. Ward and D. A. Broido, "Intrinsic Phonon Relaxation Times from First-Principles Studies of the Thermal Conductivities of Si and Ge," Phys. Rev. B, 81, 085205-1–5, 2010.

[12] P. Carruthers, “Theory of Thermal Conductivity of Solids at Low Temperatures,” Rev. Mod. Phys., 33, 1, 92–138, 1961.

[13] C. Herring, “Role of Low-Energy Phonons in Thermal Conduction,” Phys. Rev., 95, 954, 1954.

[14] P. G. Klemens, “The Thermal Conductivity of Dielectric Solids at Low Temperatures,” Proc. Roy. Soc., London A208, 108, 1951

[15] G. A. Slack and S. Galginaitis, “Thermal Conductivity and Phonon Scattering by Magnetic Impurities in CdTe,”, Phys. Rev., 133, A253, 1964.

[16] H. B. G. Casimir, “Note on the Conduction of Heat in Crystals,” Physica 5, 495, 1938.

[17] P. G. Klemens, “The Scattering of Low-Frequency Lattice Waves by Static Imperfections,” Proc. Phys. Soc. S A, 68, 12, 1113, 1955.

[18] C. A. Ratsifaritana and P. G. Klemens, “Scattering of Phonons by Vacancies,” Int. J. Thermophys., 8, 737, 1987.

[19] J. Callaway, “Model for Lattice Thermal Conductivity at Low Temperatures,” Phys. Rev., 113, 1046, 1959.

[20] P. G. Klemens, *Encyclopedia of Physics*, edited by S. Flugge, Vol. 14, p.198, Springer-Verlag, Berlin, 1956.

[21] P. B. Allen, “Improved Callaway Model for Lattice Thermal Conductivity,” Phys. Rev. B, 88, 144302, 2013.

[22] D. Douthett and S. A. Friedberg, “Effects of a Magnetic Field on Heat Conduction in Some Ferrimagnetic Crystals,” Phys. Rev., 121, 1662, 1961.

[23] S. M. Rezende, R. L. Rodríguez-Suárez, J. C. López Ortiz, A. Azevedo, “Thermal Properties of Magnons and the Spin Seebeck Effect in Yttrium Iron Garnet/Normal Metal Hybrid Structures,” Phys. Rev. B, 89, 134406, 2014.

[24] A.I. Akhiezer, V.G. Baryakhtak, and S.V. Peletminskii, *Spin Waves*, vol. 1, John Wiley & Sons, Inc, New York, 1968.

[25] J.-J. Forney and J. Jäckle, “Second Sound and Heat Conduction of Magnons in the Ferromagnetic Eu-Chalcogenides,” Phys. Kondens. Materie, 16,147, 1973.

[26] S. M. Rezende, R. L. Rodríguez-Suárez, R. O. Cunha, A. R. Rodrigues, F. L. A. Machado, G. A. Fonseca Guerra, J. C. Lopez Ortiz, and A. Azevedo, “Magnon

Spin-Current Theory for the Longitudinal Spin-Seebeck Effect," Phys. Rev. B, 89, 014416, 2014.

[27] S. M. Rezende, R. L. Rodríguez-Suárez, J. C. López Ortiz, and A. Azevedo, "Bulk Magnon Spin Current Theory for the Longitudinal Spin Seebeck Effect," J. Magn. Magn. Mater., 400, 171, 2016.

[28] S. M. Rezende, A. Azevedo, and R. L. Rodríguez-Suárez, "Magnon Diffusion Theory for the Spin Seebeck Effect in Ferromagnetic and Antiferromagnetic Insulators," J. Phys. D, 51, 174004, 2018.

[29] Y. Tserkovnyak, A. Brataas, and G. E. Bauer, "Spin Pumping and Magnetization Dynamics in Metallic Multilayers," Phys. Rev. B, 66, 224403, 2002.

[30] Y. Tserkovnyak, A. Brataas, G. E. Bauer, and B. I. Halperin, "Nonlocal Magnetization Dynamics in Ferromagnetic Heterostructures," Rev. Mod. Phys., 77, 1375, 2005.

[31] E. Saitoh, M. Ueda, H. Miyajima, and G. Tatara, "Conversion of Spin Current into Charge Current at Room Temperature: Inverse Spin-Hall Effect," Appl. Phys. Lett., 88, 182509, 2006.

[32] B. D. Cullity, *Elements of x-ray diffraction*, 3rd ed. Addison- Wesley, Reading, MA, 2001.

[33] J. Bass and W. P. Pratt, Jr., "Spin-Diffusion Lengths in Metals and Alloys, and Spin-Flipping at Metal/Metal Interfaces: an Experimentalist's Critical Review," J. Phys.: Condens. Matter, 19, 183201, 2007.

[34] Qu, S. Y. Huang, B. F. Miao, S. X. Huang, and C. L. Chien, "Self-Consistent Determination of Spin Hall Angles in Selected 5d Metals by Thermal Spin Injection," Phys. Rev. B, 89, 140407, 2014.

[35] M. B. Jungfleischa, V. Lauer, R. Neb, A. V. Chumak, and B. Hillebrands, "Improvement of the Yttrium Iron Garnet/Platinum Interface for Spin Pumping-Based Applications," Appl. Phys. Lett., 103, 022411, 2013.

[36] S. Pütter, S. Geprägs, R. Schlitz, M. Althammer, A. Erb, R. Gross, and S. T. B. Goennenwein, "Impact of the Interface Quality of Pt/YIG(111) Hybrids on Their Spin Hall Magnetoresistance," Appl. Phys. Lett., 110, 012403, 2017.

[37] K. Uchida, T. Kikkawa, A. Miura, J. Shiomi, and E. Saitoh, "Quantitative Temperature Dependence of Longitudinal Spin Seebeck Effect at High Temperatures," Phys. Rev. X, 4, 041023, 2014.

[38] R. Iguchi, K. Uchida, S. Daimon, and E. Saitoh "Concomitant Enhancement of the Longitudinal Spin Seebeck Effect and the Thermal Conductivity in a Pt/YIG/Pt System at Low Temperatures," Phys. Rev. B, 95, 174401, 2017.

[39] Cryo Industries of America, Inc., "He3 Brochure[Brochure]," Manchester, NH, 2019.

[40] G. Meunier and M. Bertaud, "Constantes Cristallographiques de $CuSe_2O_5$, $CuSeO_3$ et Cu_2SeO_4," J. Appl. Crystallogr., 9, 364−366, 1976.

[41] H. Effenberger and F. Pertlik, "F. Die Kristallstrukturen der Kupfer-(II)-oxo-Selenite $Cu_2O(SeO_3)$ (Kubisch und Monoklin) und Cu_4O-$(SeO_3)_3$ (Monoklin und Triklin)," Monatsh. Chem., 117, 887−896, 1986.

[42] J.-W. G. Bos, C. V. Colin, and T. T. M. Palstra, "Magnetoelectric Coupling in the Cubic Ferrimagnet Cu_2OSeO_3," Phys. Rev. B, 78, 094416, 2008.

[43] M. Belesi, I. Rousochatzakis, M. Abid, U. K. Rößler, H. Berger, and J.-P. Ansermet, "Ferrimagnetism of the Magnetoelectric Compound Cu_2OSeO_3 Probed by ^{77}Se NMR," Phys. Rev. B, 85, 224413, 2012.

[44] S. Mühlbauer, B. Binz, F. Jonietz, C. Pfleiderer, A. Rosch, A. Neubauer, R. Georgii, and P. Böni, "Skyrmion Lattice in a Chiral Magnet," Science, 323, 915, 2009.

[45] X. Z. Yu, Y. Onose, N. Kanazawa, J. H. Park, J. H. Han, Y. Matsui, N. Nagaosa, and Y. Tokura, "Real-Space Observation of a Two-Dimensional Skyrmion Crystal," Nature, 465, 901-904, 2010.

[46] W. Münzer, A. Neubauer, T. Adams, S. Mühlbauer, C. Franz, F. Jonietz, R. Georgii, P. Böni, B. Pedersen, M. Schmidt, A. Rosch, and C. Pfleiderer, "Skyrmion Lattice in the Doped Semiconductor $Fe_{1-x}Co_xSi$," Phys. Rev. B, 81, 041203(R), 2010.

[47] X. Z. Yu, N. Kanazawa, Y. Onose, K. Kimoto, W. Z. Zhang, S. Ishiwata, Y. Matsui and Y. Tokura, "Near Room-Temperature Formation of a Skyrmion Crystal in Thin-Films of the Helimagnet FeGe," Nat. Mater., 10, 106, 2011.

[48] S. Seki, X. Z. Yu, S. Ishiwata, and Tokura, "Observation of Skyrmions in a Multiferroic Material," Science, 336, 198 (2012).

[49] Y. Onose, Y. Okamura, S. Seki, S. Ishiwata, and Y. Tokura, "Observation of Magnetic Excitations of Skyrmion Crystal in a Helimagnetic Insulator Cu_2OSeO_3," Phys. Rev. Lett., 109, 037603, 2012.

[50] S. Seki, J.-H. Kim, D. S. Inosov, R. Georgii, B. Keimer, S. Ishiwata, and Y. Tokura, "Formation and Rotation of Skyrmion Crystal in the Chiral-Lattice Insulator Cu_2OSeO_3," PRB, 85, 220406(R), 2012;

[51] T. Adams, A. Chacon, M. Wagner, A. Bauer, G. Brandl, B. Pedersen, H. Berger, P. Lemmens, and C. Pfleiderer, "Long-Wavelength Helimagnetic Order and Skyrmion Lattice Phase in Cu_2OSeO_3," Phys. Rev. Lett., 108, 237204, 2012.

[52] H. Wilhelm, M. Baenitz, M. Schmidt, C. Naylor, R. Lortz, U. K. Rößler, A. A. Leonov, and A. N. Bogdanov, "Confinement of Chiral Magnetic Modulations in the Precursor Region of FeGe," J. Phys.: Condens. Matter, 24, 29, 2012.

[53] F. Qian, L. J. Bannenberg, H. Wilhelm, G. Chaboussant, L. M. Debeer-Schmitt, M. P. Schmidt, A. Aqeel, T. T. M. Palstra, E. Brück, A. J. E. Lefering, C. Pappas, M. Mostovoy, and A. O. Leonov, "New Magnetic Phase of the Chiral Skyrmion Material Cu_2OSeO_3," Sci. Adv., 4, 7323, 2018.

[54] A. Chacon, L. Heinen, M. Halder, A. Bauer, W. Simeth, S. Mühlbauer, H. Berger, M. Garst, A. Rosch, and C. Pfleiderer, "Observation of Two Independent Skyrmion Phases in a Chiral Magnetic Material," Nature Phys., 14, 936, 2018.

[55] M. Halder, A. Chacon, A. Bauer, W. Simeth, S. Mühlbauer, H. Berger, L. Heinen, M. Garst, A. Rosch, and C. Pfleiderer, "Thermodynamic Evidence of a Second Skyrmion Lattice Phase and Tilted Conical Phase in Cu_2OSeO_3," Phys. Rev. B, 98, 144429, 2018.

[56] P. Milde, D. Köhler, J. Seidel, L. M. Eng, A. Bauer, A. Chacon, J. Kindervater, S. Mühlbauer, C. Pfleiderer, S. Buhrandt, C. Schütte, and A. Rosch, "Unwinding of a Skyrmion Lattice by Magnetic Monopoles," Science, 340, 1076, 2013.

[57] J. Wild, T. N. G. Meier, S. Poellath, M. Kronseder, A. Bauer, A. Chacon, M. Halder, M. Schowalter, A. Rosenauer, J. Zweck, J. Müller, A. Rosch, C. Pfleiderer, and C. H. Back, "Entropy-Limited Topological Protection of Skyrmions," Sci. Adv., 3, 1701704, 2017.

[58] J. R. Panella, B. A. Trump, G. G. Marcus, and T. M. McQueen, "Seeded Chemical Vapor Transport Growth of Cu_2OSeO_3," Cryst. Growth Des., 17, 4944−4948, 2017.

[59] N. Prasai, B. A. Trump, G. G. Marcus, A. Akopyan, S. X. Huang, T. M. McQueen, and J. L. Cohn, "Ballistic Magnon Heat Conduction and Possible Poiseuille Flow in the Helimagnetic Insulator Cu_2OSeO_3," Phys. Rev. B, 95, 224407, 2017.

[60] N. Prasai, A. Akopyan, B. A. Trump, G. G. Marcus, S. X. Huang, T. M. McQueen, and J. L. Cohn, "Spin Phases of the Helimagnetic Insulator Cu_2OSeO_3 Probed by Magnon Heat Conduction," Phys. Rev. B, 99, 020403(R), 2019.

[61] L. Kong and J. Zang, “Dynamics of an Insulating Skyrmion under a Temperature Gradient,” PRL, 111, 067203, 2013.

[62] S. Lin, C. D. Batista, C. Reichhardt, and A. Saxena, “AC Current Generation in Chiral Magnetic Insulators and Skyrmion Motion Induced by the Spin Seebeck Effect,” PRL, 112, 187203, 2014.

[63] S. Gangadharaiah, A. L. Chernyshev, and W. Brenig, “Thermal Drag Revisited: Boltzmann versus Kubo,” Phys. Rev. B, 82, 134421, 2010.

[64] S. R. Boona and J. P. Heremans, “Magnon Thermal Mean Free Path in Yttrium Iron Garnet,” Phys. Rev. B, 90, 064421, 2014.

[65] R. N. Gurzhi, “Thermal Conductivity of Dielectrics and Ferrodielectrics at Low Temperatures,” Sov. Phys. JETP, 19, 490, 1964.

[66] R. A. Guyer and J. A. Krumhansl, “Thermal Conductivity, Second Sound, and Phonon Hydrodynamic Phenomena in Nonmetallic Crystals,” Phys. Rev., 148, 778, 1966.

[67] F. X. Alvarez and D. Jou, “Memory and Nonlocal Effects in Heat Transport: From Diffusive to Ballistic Regimes,” Appl. Phys. Lett., 90, 083109, 2007.

[68] S. R. Boona, R. C. Myers and J. P. Heremans, “Spin Caloritronics,” Energy Environ. Sci., 7, 885, 2014.

[69] A. V. Chumak, V. I. Vasyuchka, A. A. Serga, and B. Hillebrands, “Magnon Spintronics,” Nature Phys., 11, 453, 2015.

[70] T. Yamaguchi and H. Kohno, “Microscopic Theory of Spin-Wave Spin Torques Induced by Temperature Gradient,” J. Phys. Soc. Jpn., 86, 063706, 2017.

[71] L. Kong and J. Zang, “Dynamics of an Insulating Skyrmion under a Temperature Gradient,” PRL, 111, 067203, 2013.

[72] G. Tatara, “Thermal Vector Potential Theory of Magnon-Driven Magnetization Dynamics,” Phys. Rev. B, 92, 064405, 2015.

[73] C. Schutte and M. Garst, “Magnon-Skyrmion Scattering in Chiral Magnets,” Phys. Rev B, 90, 094423, 2014.

[74] J. H. Yang, Z. L. Li, X. Z. Lu, M.-H. Whangbo, Su-Huai Wei, X. G. Gong, and H. J. Xiang, “Strong Dzyaloshinskii-Moriya Interaction and Origin of Ferroelectricity in Cu_2OSeO_3,” Phys. Rev. Lett., 109, 107203, 2012.

[75] S. K. Kim, K. Nakata, D. Loss, and Y. Tserkovnyak, “Tunable Magnonic Thermal Hall Effect in Skyrmion Crystal Phases of Ferrimagnets,” Phys. Rev. Lett., 122, 057204, 2019.

[76] Y. Onose, T. Ideue, H. Katsura, Y. Shiomi, N. Nagaosa, Y. Tokura, "Observation of the Magnon Hall Effect," Science, 329, 5989, 297-299, 2010.

[77] C. Ulloa, A. Tomadin, J. Shan, M. Polini, B. J. van Wees, and R. A. Duine, "Non-Local Spin Transport as a Probe of Viscous Magnon Fluids," arXiv:1903.02790, 2019.

[78] M. Halder, A. Chacon, A. Bauer, W. Simeth, S. Mühlbauer, H. Berger, L. Heinen, M. Garst, A. Rosch, and C. Pfleiderer, "Thermodynamic Evidence of a Second Skyrmion Lattice Phase and Tilted Conical Phase in Cu_2OSeO_3," Phys. Rev. B, 98, 144429, 2018.

[79] S. M. Rezende, R. L. Rodríguez-Suárez, R. O. Cunha, A. R. Rodrigues, F. L. A. Machado, G. A. Fonseca Guerra, J. C. Lopez Ortiz, and A. Azevedo, "Magnon Spin-Current Theory for the Longitudinal Spin-Seebeck Effect," Phys. Rev. B, 89, 014416, 2014.

[80] S. M. Rezende, R. L. Rodríguez-Suárez, J. C. López Ortiz, and A. Azevedo, "Bulk Magnon Spin Current Theory for the Longitudinal Spin Seebeck Effect," J. Magn. Magn. Mater., 400, 171, 2016.

[81] R. Schmidt, F. Wilken, T. S. Nunner, and P. W. Brouwer, "Boltzmann Approach to the Longitudinal Spin Seebeck Effect," Phys. Rev. B, 98, 134421, 2018.

[82] L. J. Cornelissen, K. J. H. Peters, G. E. W. Bauer, R. A. Duine, and B. J. van Wees, "Magnon Spin Transport Driven by the Magnon Chemical Potential in a Magnetic Insulator," Phys. Rev. B, 94, 014412, 2016.

[83] V. Basso, E. Ferraro, and M. Piazzi, "Thermodynamic Transport Theory of Spin Waves in Ferromagnetic Insulators," Phys. Rev. B, 94, 144422, 2016.

[84] A. Aqeel, N. Vlietstra, A. Roy, M. Mostovoy, B. J. van Wees, and T. T. M. Palstra, "Electrical Detection of Spiral Spin Structures in Pt|Cu_2OSeO_3 Heterostructures," Phys. Rev. B, 94, 134418, 2016.

[85] S. Y. Huang, X. Fan, D. Qu, Y. P. Chen, W. G. Wang, J. Wu, T.Y. Chen, J. Q. Xiao, and C. L. Chien, "Transport Magnetic Proximity Effects in Platinum," PRL, 109, 107204, 2012.

[86] N. Giordano and M. A. Pennington, "Two-Dimensional Weak Localization in Combined Perpendicular and Parallel Magnetic Fields," Phys. Rev. B, 47, 9693-9705, 1993.

[87] R. Iguchi, K. Uchida, S. Daimon, and E. Saitoh, "Concomitant Enhancement of the Longitudinal Spin Seebeck Effect and the Thermal Conductivity in a Pt/YIG/Pt System at Low Temperatures," Phys. Rev. B, 95, 174401, 2017.

[88] A. Hoffmann, "Spin Hall Effects in Metals," IEEE Trans. Magn., 49, 10, 2013.

[89] S. Seki, Y. Okamura, K. Kondou, K. Shibata, M. Kubota, R. Takagi, F. Kagawa, M. Kawasaki, G. Tatara, Y. Otani, and Y. Tokura, "Magnetochiral Nonreciprocity of Volume Spin Wave Propagation in Chiral-Lattice Ferromagnets," Phys. Rev. B, 93, 235131, 2016.

[90] S. R. Boona and J. P. Heremans, "Magnon Thermal Mean Free Path in Yttrium Iron Garnet," Phys. Rev. B, 90, 064421, 2014.

[91] P. Y. Portnichenko, J. Romhanyi, Y. A. Onykiienko, A. Henschel, M. Schmidt, A. S. Cameron, M. A. Surmach, J.A. Lim, J. T. Park, A. Schneidewind, D. L. Abernathy, H. Rosner, Jeroen van den Brink, and D. S. Inosov, "Magnon Spectrum of the Helimagnetic Insulator Cu_2OSeO_3", Nat. Comm., 7, 10725, 2016.

[92] K. Ganzhorn, T. Wimmer, J. Cramer, R. Schlitz, S. Geprägs, G. Jakob, R. Gross, H. Huebl, M. Kläui, and S. T. B. Goennenwein, "Temperature Dependence of the Non-Local Spin Seebeck Effect in YIG/Pt Nanostructures," AIP Adv., 7, 085102, 2017.

[93] A. Kehlberger, U. Ritzmann, D. Hinzke, E.-J. Guo, J. Cramer, G. Jakob, M. C. Onbasli, D. H. Kim, C. A. Ross, M. B. Jungfleisch, B. Hillebrands, U. Nowak, and M. Kläui, "Length Scale of the Spin Seebeck Effect," Phys. Rev. Lett., 115, 096602, 2015.

[94] R. Schmidt, F. Wilken, T.a S. Nunner, and P. W. Brouwer, "Boltzmann Approach to the Longitudinal Spin Seebeck Effect," Phys. Rev. B, 98, 134421, 2018.

[95] V. A. Shklovskij, V. V. Mezinova, and O. V. Dobrovolskiy, "Nonlinear Relaxation Between Magnons and Phonons in Insulating Ferromagnets," Phys. Rev. B, 98, 104405, 2018.

[96] K. S. Tikhonov, J. Sinova, and A. M. Finkel'stein, "Spectral Non-Uniform temperature and Non-Local Heat Transfer in the Spin Seebeck Effect," Nat. Comm., 4, 1945, 2013.

[97] A. Prakash, B. Flebus, J. Brangham, F. Yang, Y. Tserkovnyak, and J. P. Heremans, "Evidence for the Role of the Magnon Energy Relaxation Length in the Spin Seebeck Effect," Phys. Rev. B, 97, 020408(R), 2018.

[98] I. Diniz and A. T. Costa, "Microscopic Origin of Subthermal Magnons and the Spin Seebeck Effect," New J. Phys., 18, 052002, 2016.